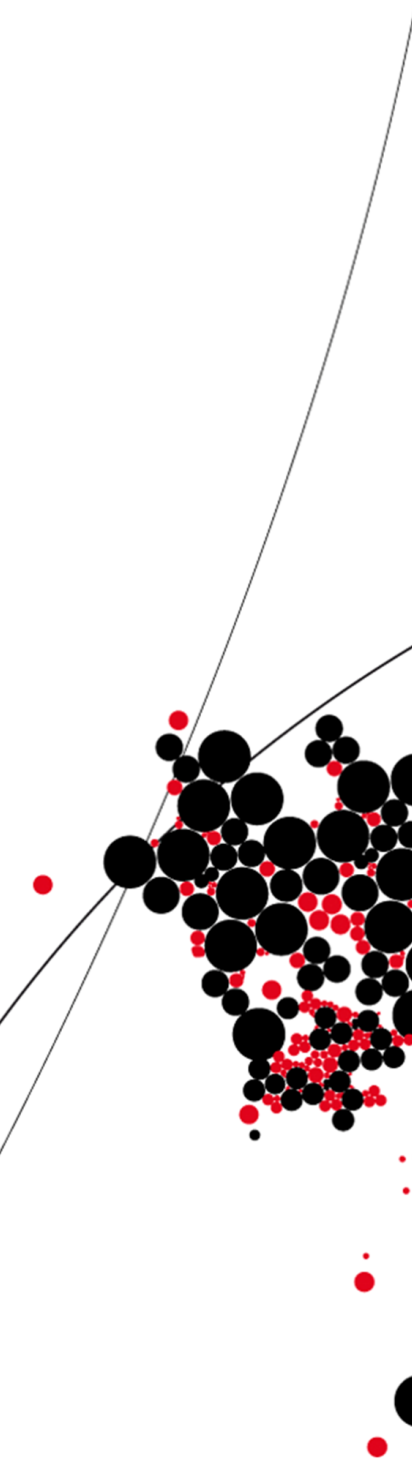




UNIVERSITY OF TWENTE.

Faculty of Science and Technology



An accessible method for measuring local SAR to assess the risk of skin-bore contact during magnetic resonance imaging.

D. Spenkelink
M.Sc. Thesis
March 2023

Supervisors:

dr. ir. W. M. Brink
prof. dr. ir. B. ten Haken
dr. ir. J. le Feber

Magnetic Detection & Imaging Group
Faculty of Science and Technology,
Technical Medical Centre,
University of Twente
7522 NH Enschede
The Netherlands

PREFACE AND ACKNOWLEDGMENTS

This thesis is the final assignment of my master Biomedical Engineering at the University of Twente. The research project is conducted at the Magnetic Detection and Imaging group. Professor dr. ir. B. ten Haken is the chairman of the graduation committee, dr. ir. W. M. Brink is the daily supervisor and dr. ir. J. le Feber is the external member of the committee.

First of all, I want to thank Wyger Brink for his guidance and supervision during the project. I think the two of us were a good team this past year. Through your guidance I learned more about the critical parts of conducting research, and I feel like I have grown a lot in the past year as an academic.

Secondly, I want to thank my family and friends for their support and belief in me throughout my university years.

And finally, I want to thank everyone I have had the privilege to learn from in the past years. I am grateful for the acquired knowledge in both the academics and in life.

ABSTRACT

The number of radiofrequency induced burn injuries due to skin contact with the bore wall of a Magnetic Resonance Imaging (MRI) scanner is on the rise and poses a threat to patient safety. To date, research on these injuries is limited to one simulation-based study. The underlying mechanism is still poorly understood, electromagnetic simulations have not been validated and the patient risk is unknown. The goal of this thesis is to develop a phantom-based method to measure local heating at skin-bore contact points to advance the research on these type of burn injuries.

Based on literature and electromagnetic simulations, the stray electric fields are identified as the potential mechanism behind skin-bore contact injuries. Through simulations, it is found that a cone phantom can be a viable replacement for a human elbow in a phantom-based skin-bore contact experiment. A novel method has been developed that can determine local heating and Specific Absorption Rate (SAR) through heat diffusion compensation on the measurements of two temperature probes. This method is likely applicable to experiments outside the context of skin-bore contact as well. These findings have been combined in an experiment on a 1.5T MRI scanner showing that the developed method can successfully measure heating and local SAR at skin-bore contact points.

Through developing an applicable method for other researchers to measure local SAR at skin-bore contact points, the incentive is hopefully renewed to continue research on this topic. For now the next challenge will be to assess the patient risk of skin-bore contact and evaluate whether current safety measures are sufficient for the coming years.

ABSTRACT [NL]

Het aantal radiofrequentie-geïnduceerde brandwonden, als gevolg van huidcontact met de boorwand van een Magnetic Resonance Imaging (MRI)-scanner, neemt toe en vormt een bedreiging voor de patiëntveiligheid. Het onderzoek naar dit type letsel is echter beperkt tot slechts één op simulatie gebaseerd onderzoek. Daarnaast blijkt het mechanisme achter deze brandwonden nog steeds niet goed te worden begrepen. De elektromagnetische simulaties zijn niet gevalideerd en het risico voor de patiënt is onbekend. Het doel van de thesis is het ontwikkelen van een fantoom-gebaseerde methode om lokale opwarming te meten op contactpunten tussen de huid en boorwand. Waardoor het onderzoek naar dit type brandwonden voort kan worden gezet.

Op basis van de literatuur en elektromagnetische simulaties worden de elektrische strooivelden geïdentificeerd als het potentiële mechanisme van het ontstaan van dit type brandwonden. Door middel van simulaties is ook gebleken dat een kegelfantoom een menselijke elleboog kan vervangen in een fantoom-gebaseerd experiment dat opwarming door contact met de boorwand nabootst. Er is een nieuwe methode ontwikkeld die de lokale opwarming en lokale Specific Absorption Rate (SAR) kan bepalen door de warmtediffusie te compenseren op basis van metingen door twee temperatuursensoren. Deze methode kan ook van toepassing zijn op experimenten buiten de context van brandwonden veroorzaakt door contact met de boorwand. Deze bevindingen zijn gecombineerd in een experiment op een 1,5T MRI-scanner, om aan te tonen dat de ontwikkelde methode met succes de opwarming en lokale SAR kan meten op een contactpunt tussen de huid en boorwand.

Door het ontwikkelen van een voor andere onderzoekers toepasbare methode om lokale SAR te meten op contactpunten tussen huid en boorwand, wordt de stimulans om verder te gaan met onderzoek naar dit onderwerp mogelijk versterkt. De volgende uitdaging zal zijn om het risico van boorwandcontact voor de patiënt in kaart te brengen en te kijken of de huidige veiligheidsprocedures nog toereikend zijn in de komende jaren.

CONTENTS

- Preface and Acknowledgments** **I**

- Abstract** **II**

- Abstract [NL]** **III**

- 1 Introduction** **4**
 - 1.1 Motivation 4
 - 1.2 Goal 6
 - 1.3 Report organisation 6

- 2 Theoretical background** **8**
 - 2.1 Basic principles of MRI 8
 - 2.2 RF transmission coil 10
 - 2.3 SAR and MRI safety standards 11
 - 2.4 RF heating and hazards 12
 - 2.5 Electromagnetic simulation of RF exposure 13
 - 2.6 Methods for measuring SAR 14

- 3 Methods** **16**
 - 3.1 Simulation of skin-bore contact mechanism 16
 - 3.2 Simplified phantom object 18
 - 3.3 Local SAR measurement 19
 - 3.4 MRI experiment 23

- 4 Results** **26**
 - 4.1 Simulation of skin-bore contact mechanism 26
 - 4.2 Simplified phantom object 29
 - 4.3 Local SAR measurement 30
 - 4.4 MRI experiment 32

- 5 Discussion** **34**
 - 5.1 Simulation of skin-bore contact mechanism 34
 - 5.2 Simplified phantom object 35
 - 5.3 Local SAR measurement 35
 - 5.4 MRI experiment 36

- 6 Future work and recommendations** **38**

- 7 Conclusion** **39**

- References** **40**

NOMENCLATURE

μ	Magnetic moment vector
\mathbf{M}	Net magnetic moment vector
B_0	External static magnetic field
\mathbf{B}_1	Radiofrequency field
ω_0	Angular frequency
γ	Gyromagnetic ratio
B_1^+	Positively rotating component of the radiofrequency field
B_1^-	Negatively rotating component of the radiofrequency field
ϵ	Permittivity
σ	Electric conductivity
ϵ_r	Relative permittivity
$T_{\text{tip}}(t)$	Tip temperature over time
$T_{\text{bulk}}(t)$	Bulk temperature over time
$T_{0,\text{tip}}$	Tip temperature at the start of the measurement
$T_{0,\text{bulk}}$	Bulk temperature at the start of the measurement
T_{room}	Room temperature
$\Delta T_{\text{tip,room}}(t)$	Change in tip temperature due to heat transfer with the room over time
$\Delta T_{\text{tip,bulk}}(t)$	Change in tip temperature due to heat transfer with the bulk over time
$\Delta T_{\text{tip,RF}}(t)$	Change in tip temperature due to RF field absorption over time
$\Delta T_{\text{bulk,room}}(t)$	Change in bulk temperature due to heat transfer with the room over time
$T_{\text{tip,room}}(t)$	Tip temperature compensated for the room temperature over time
a	Constant of decay between room and tip temperature
b	Constant of decay between bulk and tip temperature
C	Specific heat capacity

ABBREVIATIONS

MRI	Magnetic Resonance Imaging
RF	Radiofrequency
Skin-skin	Contact point between body parts
Skin-bore	Contact point between body part and bore wall
FDA	United States Food and Drug Administration
SAR	Specific Absorption Rate
NMR	Nuclear Magnetic Resonance
LP	Low Pass
HP	High Pass
BP	Band Pass
AC	Alternating Current
IEC	International Electrotechnical Commission
SAR _{10g}	SAR averaged over 10 grams of tissue
FEM	Finite Element Method
FDTD	Finite-Difference Time Domain
FIT	Finite Integration Technique
MoM	Methods of Moments
PEC	Perfect Electrical Conductor

1 INTRODUCTION

The introduction covers the motivation for this thesis, the goal and its structure.

1.1 Motivation

Magnetic Resonance Imaging (MRI) is a clinical imaging technology that produces images of the anatomy and physiological processes without the use of ionizing radiation. After its introduction in the early 1980s, the technology underwent further developments, and it is now a preferred imaging modality in a broad range of diagnostic situations. In particular, MRI has better soft tissue contrast compared to other image acquisition modalities, which is important for the diagnosis of tumours, strokes, spine lesions and cardiovascular diseases [1, 2].

Despite the relative safety of MRI scanners, patients, and individuals in the immediate vicinity of an MRI scanner can be at risk through exposure to the three types of magnetic fields: 1) the static magnetic field, 2) switching magnetic field gradients, and 3) radiofrequency (RF) magnetic fields.

1. The main hazard of the static magnetic field is its attraction of ferromagnetic materials. Ferromagnetic objects like an oxygen tank or ferromagnetic implantable devices experience a strong attractive force towards the opening of the MRI bore. In extreme cases this may lead to grave forms of bodily harm and permanent damage to devices. The static magnetic field can also induce temporary physiological effects, an example is vertigo-like sensations. However, the likelihood of serious physiological effects is exceptionally low in modern MRI scanners [3, 4].
2. The safety concerns for switching magnetic field gradients are physiological effects like peripheral nerve stimulations and acoustic noise. These effects are caused by the electric fields that are induced by the time-varying field gradients. Patients can experience discomforts and in extreme cases involuntary limb movement. There is also a risk of interaction between the switching magnetic field gradient and implants, which may result in device heating and vibration [4]. Furthermore, the gradient coils generate acoustic noise on levels that induce permanent hearing loss without the use of the required ear protection [5].
3. The main safety hazard of RF magnetic fields is tissue heating. High-power RF fields emitted by the body coil can induce currents in the body, which cause ohmic heating resulting in an unwanted rise of tissue temperature. The induced currents can concentrate at points where body parts contact each other (skin-skin), or the body's extremities contact the bore wall of the MRI scanner (skin-bore). At these points, the resulting tissue heating can lead to burn injuries [6, 7, 8]. Although operator manuals provided by the MRI vendors prescribe the placement of 1-2cm thick insulating foam pads to prevent these contact burn injuries [4], patients are still at risk due to improper patient management, as the MRI scanners are not safe-by-design [7]. RF fields can also cause tissue heating by interaction with implants or external devices [6, 7, 9].

The RF magnetic field is responsible for most of the reported injuries caused by MRI scanners [7, 10, 11]. In an analysis of 1548 adverse event reports between 2008 and 2017, the United States Food and Drug Administration (FDA) found that 906 (59%) event reports had a thermal cause. 348 (39%) of these thermal event reports had an unclear root cause for the thermal injury. 257 (28%) were caused by contact with another object. Skin-skin contact was the root cause in a total of 147 (16%) and skin-bore contact in a total of 97 (10%) thermal injury event reports [11]. Skin-skin contact typically involved the thumb and thigh making contact or the thighs with themselves, while skin-bore contact involved the elbow and bore of the MRI scanner.

In the past few decades, the prevalence of RF induced burn injuries has been on the rise and is expected to grow further in the coming years. The FDA documented 419 cases between 1997 and 2009 [7], but this has more than doubled to 906 between 2008 and 2017 [11]. This growth is expected to continue in the coming years due to the rising number of MRI scanners in service [12, 13] and due to the introduction of MRI scanners that apply higher static magnetic field strengths [14, 15, 16, 17]. As static magnetic field strength increases, so does the RF frequency, leading to greater RF heating since heating is proportional to the square of the RF frequency [10, 18, 19, 20, 21]. Thus, RF burn injuries pose a relevant threat to patient safety and must be addressed.

Several studies have sought to understand how RF burn injuries occur, these have ranged from RF heating caused by implants and external devices to skin-skin contact heating [6, 9, 22]. Two mechanisms have been described that are held culpable for excessive tissue heating by the RF field. One is the electromagnetic induction heating, occurring when the RF field induces voltages in conductive objects while the body forms a looped circuit with itself [9, 23, 24]. The other is the resonance of RF waves in implants due to the antenna effect [9, 25]. Both mechanisms induce a strong local electric field in the body and cause ohmic heating. Excessive heating due to implants, external devices and skin-skin contact can be explained through these mechanisms. Yet, they cannot explain skin-bore contact injuries, as in these cases neither implants nor a conductive loop is present.

During MRI scanning, the specific absorption rate (SAR) is monitored to ensure patient safety and prevent excessive body heating [26, 27]. SAR is a measure of the RF energy absorption rate in tissue per unit mass. The monitored SAR is a global average over the whole body or regions thereof, based on the patient's mass and the amount of delivered RF energy [26, 28]. This does not account for highly localized SAR values that can induce local burns. To assess the risk on burn injuries and understand underlying RF burn mechanisms, precise local SAR measurements are necessary.

Computer simulations of the electromagnetic field inside an MRI scanner can be used to estimate the localized SAR values in human models [29]. These simulations have been widely utilized to analyse RF heating [6, 28, 30], notably with implants and external devices to investigate MRI compatibility in terms of RF heating [31, 32, 33]. Simulations are a cost-efficient and time-saving substitute to experiments. They are, however, simplifications of reality since it is not feasible to accurately replicate the intricate human structure and the RF field generated by an RF transmission coil [34]. Therefore, results of simulations should be validated by analytical results or experimental measurements to be reliable.

Despite that skin-skin and skin-bore contact injuries are the cause of 26% of the thermal event reports [11], there has only been one simulation-based study that has focused on these types of injuries. In the study by Tang et al. [6], the authors simulated burn injuries at both the skin-skin and skin-bore contact locations. They confirmed the mechanism of loop formation for the

skin-skin contact injury but failed to define a mechanism that would lead to skin-bore contact injuries. The study did find that the local SAR in skin-bore cases is affected by the position of contact and is consistent with the electromagnetic field distribution.

However, Tang et al.'s study [6] has a key weakness; the simulation results are not validated by analytical or experimental results. The electromagnetic properties and simulated SAR are known to be dependent on the design of the body coil [35]. But in Tang et al.'s study, a simplified body coil design was used to speed up the simulations, which could cause additional discrepancies in the simulation results. Therefore, the degree of risk for patients in these contact cases is still uncertain.

Since skin-skin contact injuries are better documented and understood [24, 36, 37, 38], this thesis will seek to advance the research on skin-bore contact injuries as yet little is known about the mechanism and risk. To date, no studies have been conducted that validate simulation results with, or which involve experiments in an MRI scanner. Therefore, a phantom-based method will be developed, which can replicate and measure the local SAR that occurs in a patient's elbow during bore wall contact. The method is intended to be accessible and applicable by other researchers and MRI technicians who want to measure the local SAR at the bore wall to investigate patient risk or validate skin-bore contact simulations.

Developing this method will pose challenges. Since the patient risk is unknown for skin-bore contact cases, a phantom must be used instead of volunteers for safety considerations. The phantom will be a simplified version of a human body, as it is not feasible to replicate the complexity or the entirety of the human body. Thus, to develop a phantom that can accurately replicate the characteristics of an elbow, the mechanism of skin-bore contact injuries must be understood to know which phantom characteristics are of importance. Additionally, a method of measuring local SAR needs to be established. Through this method a first indication of heating intensity at the skin-bore contact point can be determined.

1.2 Goal

The goal of this thesis is to develop a phantom-based method to measure local SAR at skin-bore contact points in an MRI scanner and test the method through the identification of the highest contact heating in an MRI scanner. To obtain this goal, multiple specific research questions have to be answered:

1. What is the mechanism behind skin-bore contact injuries?
2. What phantom object can replicate the characteristics of a human elbow in a skin-bore contact case?
3. What is a feasible method to measure local SAR at the skin-bore contact point?
4. Where on the MRI bore would a patient experience the highest contact heating?

1.3 Report organisation

The main structure of the thesis consists of seven chapters. Chapter one is the introduction, chapter two provides the information for a better understanding of the topics in this thesis. Chapter three outlines the research methodology and chapter four provides the results. Chapter five, six, and seven cover the discussion, future work and recommendations, and conclusion.

The research in this thesis is conducted in sequence. Each research question is answered in turn, leading closer to achieving the thesis goal. Therefore, the methods for research questions two, three and four are based on the results of the preceding research questions.

2 THEORETICAL BACKGROUND

This chapter provides a deeper overview of the topics introduced in the previous chapter. It covers the fundamental principles of MRI, the RF transmission coil, MRI safety standards and how RF exposure induces tissue heating - an initial exploration of the first research question through existing literature is included. A look into electromagnetic simulation of RF exposure and methods of measuring local SAR is also provided.

2.1 Basic principles of MRI

MRI is based on the principles of nuclear magnetic resonance (NMR), which is concerned with the nuclear spin of atoms. All nuclei are built out of protons and neutrons and therefore positive of charge. Additionally, nuclei with either an odd atomic number or an odd mass number have an angular momentum and thus a nuclear spin. These nuclei are NMR active. The hydrogen nucleus is NMR active, consisting of one proton and zero neutrons, giving it an atomic number of one resulting in a nuclear spin. Coupled with their high abundance in the human body, makes them perfect for MRI [39].

A hydrogen nucleus can be seen as a small sphere of distributed positive charge that spins with a certain frequency around its axis due to the angular momentum or spin. Therefore, the nucleus must contain a magnetic field since a magnetic field is present whenever there is a circulating charge according to Faraday's induction law. This microscopic magnetic field has a magnetic moment μ . A group of nuclei has a net magnetization \mathbf{M} [39].

Without an external magnetic field, the μ of nuclei orientate in random directions within the body. When an external static magnetic field B_0 is applied, μ will try to align with B_0 . But as the nuclei have an angular inertia from their spin, they will resist the directional change in rotation. The resulting force of B_0 on μ creates a torque, which deflects μ into a circular path around the direction of B_0 . The rotation of μ under an angle with B_0 is called precession. The precession phenomenon has a frequency and precession angle. However, the bulk magnetization \mathbf{M} does align with B_0 as in a vector sum of a large group of μ the precessed angles will cancel out. The magnetic interactions of the bulk magnetization \mathbf{M} comply with classical mechanics, which is sufficient for understanding the basic principles of MRI [39, 40].

When a sample is in the presence of B_0 for some period, the net \mathbf{M} aligns parallel with B_0 , which is known as the longitudinal or equilibrium state. During imaging, energy is added to the collection of nuclei which causes \mathbf{M} to tip away from its initial longitudinal direction, creating nonzero transverse magnetization. The angle between \mathbf{M} and B_0 is known as the flip angle. The action of tipping \mathbf{M} away from equilibrium is called excitation. Maximum transverse magnetization is generated when the flip angle is 90° or $\pi/2$ [39, 41].

The time-varying magnetic field \mathbf{B}_1 is the RF magnetic field transmitted by an MRI scanner for the excitation of \mathbf{M} . To apply a flip angle to \mathbf{M} it is important that \mathbf{B}_1 's frequency resonates with

the angular frequency of the hydrogen nucleus. This resonance frequency is proportional to the strength of B_0 and described by the Larmor's equation

$$\omega_0 = 2\pi\gamma B_0 \quad (2.1)$$

where ω_0 is the angular frequency of the hydrogen nucleus, also known as the Larmor frequency. γ is the gyromagnetic ratio, a constant specific for each type of atomic nucleus. For the hydrogen nucleus, the gyromagnetic ratio is equal to 42.58 MHz/T. B_0 is the static magnetic field strength expressed in the unit Tesla [39, 41, 42].

The \mathbf{B}_1 field can be distinguished in positively and negatively rotating circularly polarized components, respectively B_1^+ and B_1^- . Polarization is the orientation of a time-varying magnetic field vector in a plane. The characterization of polarization is dependent on the two perpendicular components of the magnetic field vector and their phase difference. Circularly polarization is characterized by the perpendicular components having equal amplitudes and the components being 90° or $\pi/2$ out of phase. A circularly polarized vector can thus be visualized as a constant vector that circles in a plane, which is a necessary property of \mathbf{B}_1 for the excitation of \mathbf{M} [41, 43].

For excitation, a circularly polarized component of \mathbf{B}_1 must be applied perpendicular to \mathbf{M} in the transversal plane of B_0 at the Larmor frequency, as can be seen in Figure 2.1. Once \mathbf{M} is excited, the rotational direction of \mathbf{M} in the transversal plane is described by the right-hand-rule. Following the B_0 direction with the right-hand thumb, it can be seen that \mathbf{M} will rotate along the curl of the fingers in counterclockwise direction, which is known as positively rotating. B_1^+ is the positively rotating component of \mathbf{B}_1 that will excite \mathbf{M} . Therefore, B_1^+ is defined as the transmit RF field. B_1^- is pertinent for signal reception and defined as the receive RF field. Once \mathbf{M} is excited, the transverse component of the magnetization can be measured as a rotating magnetic field or B_1^- , which induces a detectable voltage in a nearby inductive coil according to Lenz's law [39, 41, 42].

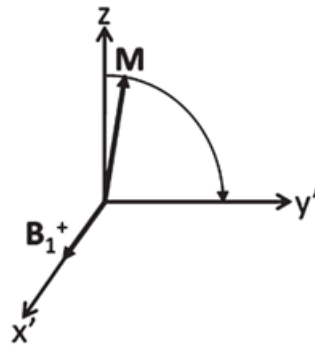


Figure 2.1: The circularly polarized component B_1^+ of the RF magnetic field \mathbf{B}_1 induces a precession of \mathbf{M} . The static magnetic-field B_0 is oriented along the z-axis. The $x'y'$ -plane is a rotating frame of reference rotating counterclockwise at the Larmor frequency. Note that for every flip angle of \mathbf{M} , B_1^+ stays perpendicularly orientated.

In addition to the B_0 and B_1^+ magnetic fields, a third type of magnetic field is applied during MRI scanning: magnetic field gradients. As was discussed earlier, the Larmor frequency is proportional to the strength of B_0 . By applying a magnetic field gradient to the static magnetic field B_0 along all three axes, it is possible to encode spatial information into the frequency and phase of the spins [39]. However, for this thesis the magnetic field gradients are not relevant as they do not contribute to tissue heating. Therefore, they will not be discussed further.

It is also useful to clarify the x, y, and z-axis directions used in MRI. The x-axis of an MRI patient runs between the left and right side, y-axis between front and back, and the z-axis between the head and feet [39].

Thus, in MRI three magnetic fields are required for imaging. This thesis will focus on the thermal hazards related to RF exposure by the B_1^+ field. Therefore, the subsequent sections go into RF transmission coils, their associated safety considerations, and the role of electromagnetic field simulations.

2.2 RF transmission coil

The goal of the RF coils is to transmit and receive RF signals. Most clinical MRI systems use separate coils for each of these functions, but they can also be combined in transmit/receive coils. There are two basic types of RF coils: surface and volume coils. Surface coils are placed near the to-be-imaged region and offer a superior receive sensitivity close to the coil. Volume coils surround the region that is imaged and provide a highly uniform sensitivity across their volume. Clinical MRI systems typically use a body-sized volume coil integrated behind the bore liner for RF transmission, in addition smaller volume coils can be used around a specific anatomic region of interest such as the knee or head. In this thesis, the so-called birdcage volume coil design is of interest, which is most often used in modern MRI scanners, and the relevant RF transmission coil in skin-bore injury cases [39, 44].

The birdcage RF resonator coil design was first proposed in 1982 by Cecil E. Hayes; as an improved alternative over conventional saddle coils and slotted tube resonators [45, 46]. The construction of a birdcage coil consists of two circular conductive loops called “end-rings” connected by an even number of conductive straight elements called “rungs”, typically 8 to 32. The conductive parts of the birdcage are segmented by capacitors. Dependent on the location of the capacitors, three types of birdcages can be defined: low pass (LP), high pass (HP) and band pass (BP). An LP design has capacitors on the rungs, HP has capacitors on the end-rings and BP has capacitors on both the rungs and end-rings [47, 48]. A schematic of a HP birdcage coil design can be seen in Figure 2.2.

The birdcage coil is a resonant circuit that transmits the B_1^+ time-varying magnetic field when an alternating electric current is applied over the circuit. To match the resonant frequency of the coil to the Larmor frequency, the coil must be tuned [44, 48]. Tuning is achieved by adjusting the capacitance of the capacitors to obtain a uniform B_1^+ field with the correct frequency [29, 49]. Thus, the capacitors are an essential part of the birdcage coil.

A birdcage coil design can be driven in quadrature to generate a circularly homogenous polarized B_1^+ field. Quadrature transmission in the first resonance mode is achieved by powering the birdcage coil by two sinusoidal electric currents with a phase difference of $\pi/2$ radians through two alternating current (AC) feeding ports located on the end-ring under a $\pi/2$ radians angle [44, 45, 48]. The first resonance mode of a birdcage is achieved when the total phase shift around the circumference of the end-ring is equal to 2π radians. Higher order modes have a total phase shift of an increasing multiple of 2π radians and are progressively more inhomogeneous [46, 47].

Limits for the absorption of the RF coil's transmitted B_1^+ field are issued by the regulatory bodies to prevent excessive heating of body tissue. These standards are discussed in the following section.

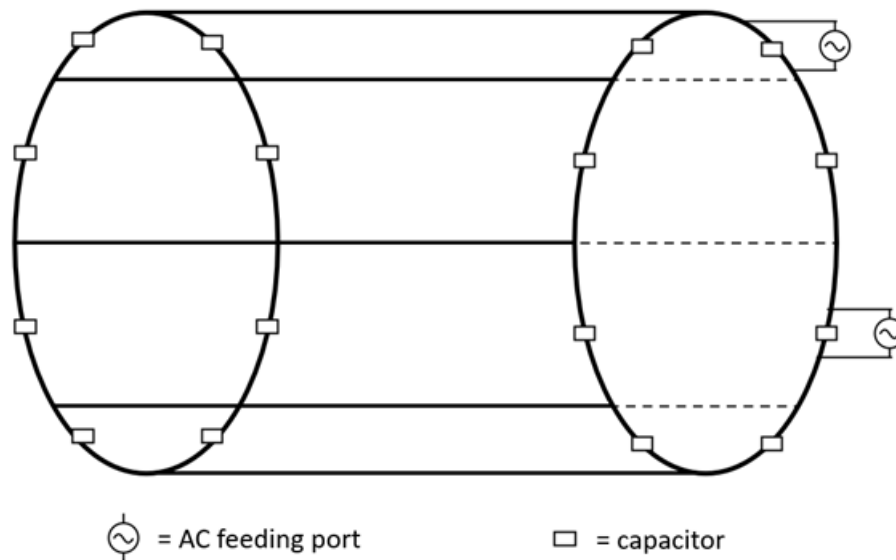


Figure 2.2: Schematic of an 8-rung HP birdcage coil design. The capacitors are located on the two end-rings, two AC ports placed under a $\pi/2$ radians angle feed current to the birdcage.

2.3 SAR and MRI safety standards

The International Electrotechnical Commission (IEC) [50] performs risk evaluation and offers guidance on protection against non-ionizing radiation such as static and low-frequency electric and magnetic fields, RF fields, and microwaves. The IEC specifies the regulatory limits that are relevant within the European Union.

RF safety limits in MRI are defined in terms of SAR (39). SAR represents the rate at which energy is absorbed by a biological object exposed to electromagnetic fields and is expressed in the unit 'W/kg'. Different averaging schemes are used to address different exposure locations and scenarios. These averaging schemes can be divided in global SAR and local SAR [27].

Global SAR is defined as the SAR averaged over the exposed body section, which can be either the whole-body, partial body, or the head. It can be linked to the total RF power that is accepted by the configuration. Local SAR is defined as the peak SAR value after averaging over 10 grams of tissue (SAR_{10g}), where different limits are employed for head/torso and extremities [27]. Unlike global SAR, local SAR cannot be monitored by the total accepted RF power, as it is a complex function of anatomy and proximity to RF sources [43]. Predictions of local SAR are typically made by linking the global SAR to the evaluation of multiple generic body models with safety margins to ensure compliance in all subjects [28]. Local SAR safety limits only apply to surface coils and not to body coils, even though it is known that body coils can induce burn injuries caused by a high intensity of local SAR [11, 36, 37, 38].

The global and local SAR limits specified by the IEC are shown in Table 2.1. The IEC defines two control modes with increased SAR limits in addition to the normal mode: the first and second control mode. For the first control mode medical supervision is necessary and for the second control mode explicit authorization of the local investigational review board [27, 43]. To reduce the risk of causing unwanted local tissue heating at skin-bore or skin-skin contact points, the MRI industry has developed safety procedures where non-conducting pads are positioned to

prevent the patient from direct contact with the bore wall or with itself. These pads are placed between skin-skin and skin-bore contact locations. The pad thickness is recommended to be between 1 and 2 centimetres [4, 43].

Table 2.1: Overview of global and local SAR limits as specified by the IEC. *The partial body SAR scales with the ratio of exposed patient mass to patient mass between the defined limits [27].

Safety Parameter		IEC 60601-2-33 Normal Mode	IEC 60601-2-33 First Control Mode	IEC 60601-2-33 Second Control Mode
Global SAR	Whole Body SAR	$\leq 2\text{W/kg}$	$\leq 4\text{W/kg}$	$> 4\text{ W/kg}$
	Partial Body SAR*	$\leq (2 - 10)\text{W/kg}$	$\leq (4 - 10)\text{ W/kg}$	$> (4 - 10)\text{ W/kg}$
	Head SAR	$\leq 3.2\text{W/kg}$	$\leq 3.2\text{W/kg}$	$> 3.2\text{ W/kg}$
Local SAR	Head/Torso SAR	$\leq 10\text{ W/kg}$	$\leq 20\text{ W/kg}$	$> 20\text{ W/kg}$
	Extremities SAR	$\leq 20\text{ W/kg}$	$\leq 40\text{ W/kg}$	$> 40\text{ W/kg}$

The following section will discuss how SAR is induced by the B_1^+ field's interaction with the body, in particular the mechanisms that can induce high local SAR. A possible answer to the first research question regarding the mechanism behind skin-bore contact injuries is assessed from the literature.

2.4 RF heating and hazards

The time-varying B_1^+ field has like all electromagnetic radiation a time-varying electric and time-varying magnetic field component. Both these components interact with the body during RF exposure and can induce heating [51].

The interaction of the time-varying electric field component with the human body results in electric currents and the reorientation of electric dipoles that induce dielectric losses. These interactions result in an absorption of the B_1^+ field and heats up the body's tissue. The magnitude of these different effects depends on the type of tissue and on the frequency of the applied time-varying electric field [51, 52, 53]. Patients are vulnerable to heat stroke when their bodies cannot regulate their core temperature due to excess heat absorption. The global SAR can predict the rise in core temperature and global SAR limits can adequately prevent an excessive core temperature rise [27].

The time-varying magnetic field component can induce circulating electric currents within a conductive volume. As the human body is a reasonable conductor, due to the presence of ions, it is susceptible to the time-varying magnetic field. The magnitude of the currents is proportional to the radius of the current loop; thus, the strongest currents are induced where the loop dimensions are the greatest. Strong induced currents are found in obese patients or in cases where the body forms an inductive loop with itself, such as thumb-thigh or thigh-thigh contact cases. These currents will deposit substantial amounts of thermal energy at the point of highest resistance, which is typically the skin-skin contact point, resulting in a high local SAR [51, 52].

Although the exact mechanism behind skin-bore contact injuries is unclear, the placement of insulating pads has been prescribed as a preventative measure. But different institutions mention different reasons for using pads. The British Medicines and Healthcare products Regulatory

Agency states that pads should prevent the patient's skin touching the bore of the magnet, or come within 1cm of touching [4]. The American College of Radiologists states that pads must be placed to protect the patient from proximity to the transmit RF coil [54]. The British College of Radiographers and the Australian and New Zealand College of Radiologists both prescribe pads to prevent patient contact with the bore wall [55, 56].

So, there is agreement that contact with the bore wall should be prevented, but it is not clear whether close proximity to the RF transmission coil or contact with the bore wall is the cause of skin-bore contact injuries.

It was a review article by Cecil E. Hayes [46], wherein he gives a personal account on the hardships that challenged him during development of the birdcage resonator, which gave a strong clue to the mechanism behind skin-bore contact injuries. In this article, Hayes discusses the problem of stray electric fields near the bore wall, that can cause excessive dielectric losses if a patient rests their arm against the bore wall. These fields are generated by stray capacitance between the birdcage coil's capacitors and a nearby electric conductor, like the human body. The radial components of the stray electric field extend inward the birdcage by approximately the gap distance of the capacitor, sufficient of a distance for patients to experience local heating [29, 43, 46].

It should be mentioned that in approximately 1985, during development of the first birdcage resonator, a 'short-term solution' was introduced to protect against stray electric fields by placing insulating pads between the patient arms and bore wall [46]. Almost 40 years later this 'short-term solution' is still used [4, 54, 55, 56].

In this thesis, the hypothesis that stray electric fields induce a high local SAR at the bore wall is tested. Electromagnetic simulations are conducted to confirm the mechanism of skin-bore contact injuries. This is done by investigating the influence of the contact location along the bore wall on the local SAR, and whether introducing a gap between the elbow and bore wall affects the local SAR. If stray electric fields are the cause, it is expected that the highest local SAR is found near the capacitors on the bore wall, and that skin-bore contact is unnecessary for high local SAR, as the stray fields can move inward the birdcage independently of bore wall contact.

How electromagnetic simulations work is explained in the following section.

2.5 Electromagnetic simulation of RF exposure

Electromagnetic simulations with anatomical body models can be used to evaluate RF exposure scenarios and predict local SAR. These simulations are typically performed with commercially available software packages. They provide features such as computer-aided design tools, libraries with a wide range of materials and a range of excitation sources to design simulations with. Post-processing tools can calculate SAR from the simulated electric fields [29].

The simulation software packages can be based on various numerical methods such as the Finite Element Method (FEM), Finite-Difference Time Domain (FDTD), Finite Integration Technique (FIT) and Methods of Moments (MoM). Widely used software packages are COMSOL [57], Sim4-Life [58] and CST studio suite [59], which use FEM, FDTD and FIT/FEM respectively to obtain solutions for Maxwell's equations. In this thesis CST studio suite will be used with the time domain solver, which uses the FIT numerical analysis method [29, 59, 60].

For solving the equations underlying the FIT, a finite computational domain is defined, which encloses the volume of interest as well as the RF field sources. Subsequently, a staggered mesh grid discretizes the domain in small elements or grid cells. Computational power will increase with a higher amount of grid cells in the simulation domain [61].

The FIT method applies update equations derived from the integral forms of the first two Maxwell equations: the Faraday's induction law and Ampère-Maxwell's circuit law. The material properties used in the update equations are the permittivity (ϵ) and electric conductivity (σ). Knowing the media parameters of the local grid cells and previous electric field and magnetic field values, the update equations can calculate the next-in-time electric field values from the previous magnetic field in the staggered grid. From the calculated electric field, the subsequential magnetic field is calculated. This becomes an iterative loop until a certain convergence criterion is met [61, 62, 63].

However, simulation results are susceptible to biases and cumulative errors [6, 34]. Therefore, to estimate the accuracy of the simulation in vivo and human experiments are indispensable. The methods for measuring SAR in this type of experiment are discussed in the following section.

2.6 Methods for measuring SAR

Modern MRI scanners can estimate partial SAR by linking the global SAR to numerical evaluations of generic body models, but these estimations tend to be unreliable [28]. The accurate calculation of SAR is difficult as it is dependent on factors as patient size, heterogeneity of tissue conductivity and differences in RF power distribution profiles. It has also been found that SAR values indicated by MRI scanners may not be reliable [64, 65, 66], while clinical users have limited to no independent methods for the validation or verification of the predicted SAR by the MRI scanner manufacturers [66, 67].

RF dosimeter prototypes have been proposed as scanner-independent devices for measuring average SAR over body parts [64, 65, 68, 69], yet these devices are not suitable for measuring the local SAR at skin-skin and skin-bore contact locations.

Local SAR measurements, used in both the MRI and wireless telecommunications industries, are typically conducted with electric field probes [67]. These probes measure the electric field vectors in three orthogonal directions inside a phantom that is modelled to imitate human tissue [70]. Local SAR can be calculated as a function of electric conductivity, volumetric density, and the measured electric field vector [67, 71].

As local SAR is linked to temperature change in tissue, it can also be measured using temperature probes [72, 73]. When RF exposure is short, local SAR can be estimated from the initial temperature change. This is useful in the telecommunications industry, but this is not feasible in MRI due to the longer scan times. As then the issue of heat diffusion is introduced, making temperature change not proportional to local SAR due to the diffusion of RF energy [74].

A novel method for calculating local SAR has been proposed for MRI that uses high resolution 3D temperature mapping [75]. This method computes the local temperature change of a phantom before and after RF exposure using proton frequency shift [76]. Values for the local SAR are then determined by solving the inverse heat equation with the temperature difference map and thermal properties, which accounts for heat diffusion during extended RF exposure. MRI thermometry has been used before to create temperature difference maps to validate phantoms

for accurate RF field characterizations [77].

3 METHODS

This chapter outlines the methods used to answer the research questions and achieve the thesis goal. Section one covers electromagnetic simulations of the skin-bore contact mechanism. Section two focuses on designing a phantom to mimic a human elbow in a skin-bore contact case. Section three introduces a novel local SAR measurement method and section four discusses an MRI experiment to find the location of highest RF heating on the bore wall.

3.1 Simulation of skin-bore contact mechanism

Research question 1 seeks to identify the mechanism behind skin-bore contact injuries. In Section 2.5, literature was found that suggested stray electric fields as a possible mechanism. To confirm this, electromagnetic simulations will be conducted. If stray electric fields are the issue, it is expected that the highest local SAR will be found near the capacitors on the bore wall and that skin-bore contact is not necessary for high local SAR, as the stray fields can move inward independently of the bore wall towards nearby conductors.

The electromagnetic simulations are performed with the time domain solver in the CST Microwave Studio software package [59]. The simulation computes the system at the Larmor frequency 64MHz of a 1.5T MRI scanner. The boundaries of the simulation system are open to prevent signal reflection by the boundary. The convergence criterion of the time domain solver is set to -20dB, which means that the solver stops when the energy in the computational domain has decreased by 20dB. Maximum cell size of the mesh grid is 10 cells per wavelength and the minimum cell size is 5mm. The mesh grid is refined in areas where local geometrical details are important, in this case the skin-bore contact point.

A non-resonant HP birdcage model with 16 rungs is used to simulate a body coil. This model makes use of multiport excitation, which ensures that the currents inside the coil have a specific amplitude and phase. It does not incorporate lumped elements like resistors and capacitors that are applied in physical coils [35, 78], a schematic of the coil can be seen in Figure 3.1a. Advantages of a multiport excitation model are the low computational cost and that tuning the capacitors to the Larmor frequency is not required [35]. It was found that a 16-rung non-resonant HP birdcage model simulates the electric field accurately, aside from a specific region in the middle of the rungs [35]. This is acceptable as the capacitors, and thus the stray electric field locations, are positioned on the end-rings and not on the rungs. However, it should still be considered in the discussion of the results.

The computational birdcage model is built in the CST Microwave Studio software package [59] with a rung length of 520mm. Both end-rings (radius: 305mm) have gaps for the multiport excitation between the connections of the end-ring and rungs. The rung and end-ring elements have a width of 10mm and are made from perfectly electrical conductor (PEC) material. The birdcage coil is modelled to simulate the transmission of a quadrature RF field in the first resonance mode. The coil model in CST Microwave Studio can be seen in Figure 3.1b.

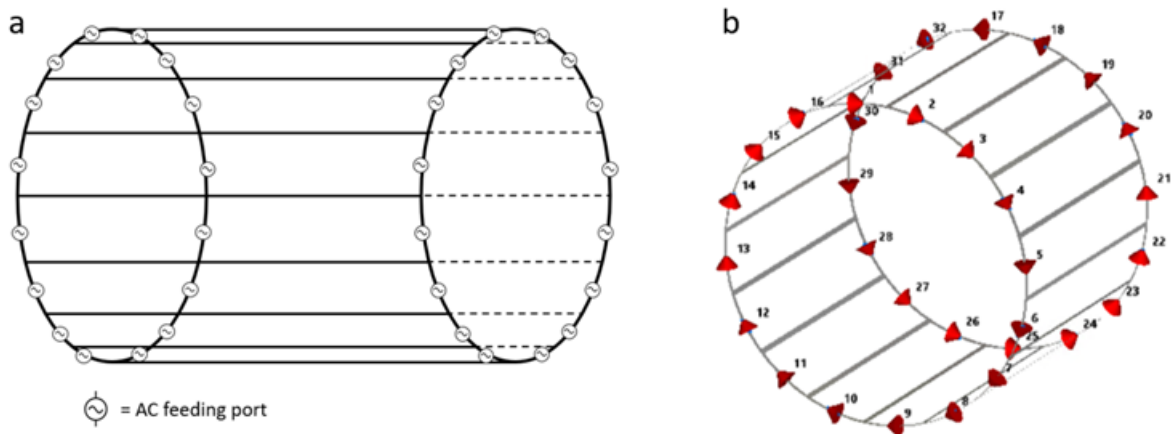


Figure 3.1: a) Schematic of a 16-rung HP birdcage model; b) a 16-rung HP computational birdcage model in CST.

The birdcage model additionally consists out of an RF shield and bore wall. The RF shield (radius: 335mm, length: 1000mm) is made from PEC and the bore wall (radius: 290mm, thickness: 5mm, length: 1000mm) is made from fibre-reinforced plastics (ϵ_r : 5.5, σ : 1×10^{-14} S/m), ϵ_r is the relative permittivity [6].

The body phantom used in the simulations is theposable Gustav 2.0 2mm model from the CST Voxel Family [79]. The choice for this specific body model is made as this model's posture is adjustable through the CST Human Phantom Poser function. This is important since the elbow of the body model must be placed on the bore wall to mimic the skin-bore contact burn injury cases. The Gustav body model has a mass of 69kg and is composed of 79 tissue types. The main body tissues that constitute the elbow are skin, muscle and cortical bone [80].

The body phantom is posed with the right arm in the original position along the body. Care is taken to ensure that the lower arms do not contact the body to prevent the creation of conducting loops in the body. The left upper arm is positioned above the body in a way that the elbow is able to contact the bore wall. From the original body pose of the Gustav model, only two joints are adjusted to obtain the desired pose: the left shoulder joint (rotation: $x=-38^\circ$, $y=21^\circ$, $z=0^\circ$) and the left elbow joint (rotation: $x=0^\circ$, $y=-80^\circ$, $z=0^\circ$).

The standard position of the body phantom has the head towards the positive side of the z-axis along the B_0 field direction with the elbow positioned on the MRI bore wall at $z=0$ mm, which is the centre of the birdcage along the z-axis. This position can be seen in Figure 3.2. The bore wall contact point is made sure to be aligned with the birdcage ports, for the stray electric field is expected to peak in the closest proximity to the capacitors.

Local SAR values are calculated with an averaging mass of 10 grams as prescribed by the IEC [27] and projected on the body model. The calculated local SAR values are normalised to the maximum allowed average power in the normal mode. The whole-body SAR limit in the normal mode is 2W/kg [27]. The B_1^+ field strength is monitored at the isocentre of the scanner (coordinates: 0,0,0), this value is dependent on the size and material characteristics of the object inside the birdcage. The system will have to increase RF power transmission for a heavier object or a material with a higher permittivity to achieve the 2W/kg whole-body SAR limit, which can influence the power dissipation of the RF field at the skin-bore contact point.

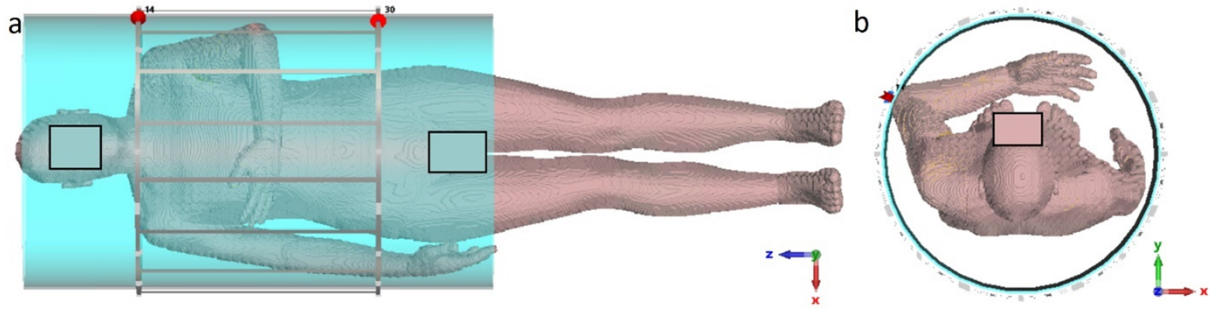


Figure 3.2: a) Top view, and b) side view of the standard position of the Gustav model inside the computational 16-rung HP birdcage. The transparent blue object is the bore wall. Only ports 14 and 30 are shown to indicate that the elbow is positioned along the line between the birdcage ports.

Therefore, it can be instructive to compare B₁₊ field centre values to indicate whether the local SAR at the contact point is influenced by the intensity of the transmitted B₁₊ field, instead of the position of the contact point or birdcage type. Studies by Tang et al. [6] and Murbach [43] also normalise to an 1 μ T centre B₁₊ field strength, but this will not be applied. As the normalisation to 2W/kg whole-body SAR is considered to be sufficient to answer the research questions.

Simulations are conducted to study the influence of skin-bore contact point position on local SAR. The Gustav body model is shifted 65mm, 175mm, 205mm, 225mm, 250mm, 255mm, 275mm, 300mm, 325mm and 345mm from the standard position towards the positive z-axis direction. Additionally, to explore the importance of contact with the bore wall for high local SAR, the phantom is shifted 10mm, 20mm, 30mm and 40mm from the bore wall in the direction of the positive x-axis at a z-position of 250mm, chosen as here the elbow is directly in front of a capacitor. Also, a simulation of an empty birdcage scanner is conducted. The simulation results are presented in Section 4.1.

3.2 Simplified phantom object

Research question 2 is about finding a simplified phantom that can mimic the RF absorption characteristics of a human elbow in a skin-bore contact case. Because, using human volunteers is not an option due to the unknown risk of burn injuries and creating a replica of a human elbow is too complex to achieve given the resources available. Nor is it feasible to replicate the elbow of the Gustav body phantom which consists out of 79 tissue types [80].

Results from Section 4.1 showed that the mechanism behind skin-bore contact injuries are the stray electric fields induced by the capacitors of the birdcage. To simplify the phantoms, three steps are taken: simplification of the body phantom, disconnecting the elbow from the torso, and replacing the elbow with a cone geometry. As stray electric fields at the contact point are the main source of heating, it is hypothesized that the adjustments made to the phantoms at the contact point affect the heating most. Therefore, disconnecting the elbow from the torso has likely little effect on the heating. The simplified phantoms can be seen in Figure 3.3.

For the first simplification phantom, the ‘arm phantom’, the Gustav body model is replaced by a cylinder (radius: 145mm; length: 1000mm) at the centre of the birdcage. The arm contacting the bore wall is made out of two cylinders (radius: 35mm) under a 90° angle connected by a sphere (radius: 35mm) to mimic an elbow joint. The arm is connected to the body cylinder. All

components are made from the Gustav muscle biomaterial (ϵ_r : 55.03; σ : 0.943S/m) and have a total mass of 72.777kg.

The second simplified phantom, the 'elbow phantom', is constructed by shortening the upper and lower arm length to 35mm, resulting in a detachment from the body cylinder. It has a mass of 71.653kg.

For the last simplified phantom, the 'cone phantom', the elbow phantom is replaced by a geometric object as emphasis is put on the ability to reproduce the phantom for an MRI experiment. A cone geometry (top radius: 5mm, bottom radius: 60mm, height: 100mm) is used as the small top radius can mimic the bore wall contact point and the wide bottom can function as the elbow's mass. The cylinder mimicking the body is still in place and the cone makes no contact with the cylinder. All segments are made from the Gustav muscle biomaterial. The total mass of the phantom is 71.780kg.

The characteristics of the simplified phantom designs are evaluated with simulations. The phantoms are simulated with a contact point at a z-position of 250mm in front of a capacitor, as stray electric field strength is strongest at this location. To evaluate the phantoms, peak SAR_{10g} on the contact surface and the centre B₁⁺ field intensity are computed, based on the simulation methods from Section 3.1.

The simulation results can be seen in Section 4.2.

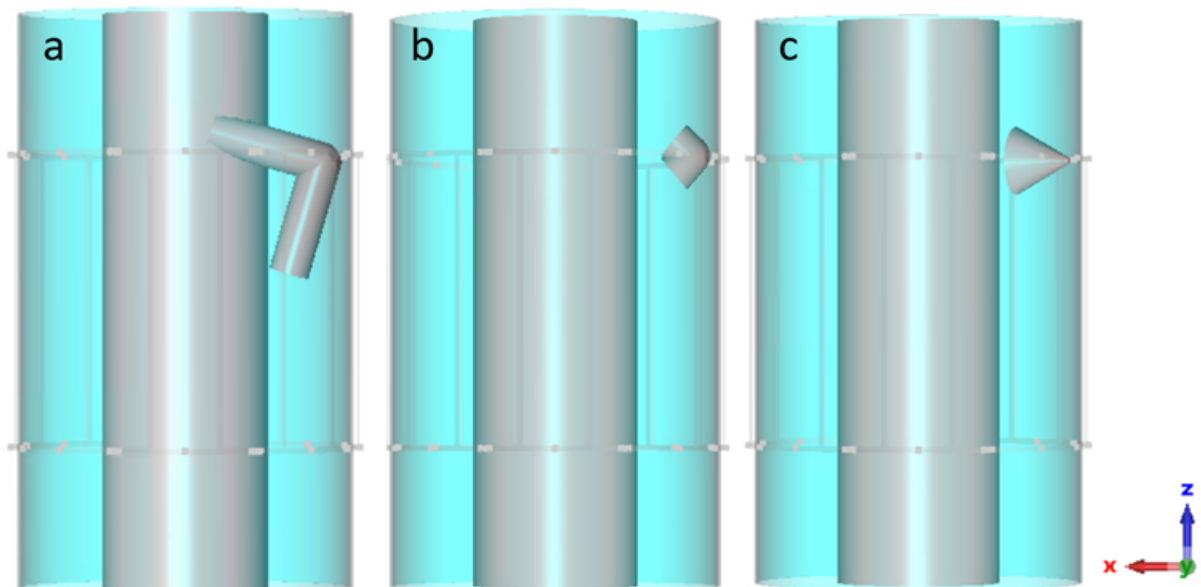


Figure 3.3: Top view of a) the simplified arm phantom, b) the simplified elbow phantom and c) the cone phantom inside the 16-rung non-resonant HP birdcage. The transparent blue object is the bore wall.

3.3 Local SAR measurement

Research question 3 is about finding a feasible method for measuring local SAR. In Section 2.6, three methods are provided for local SAR measurements. In this thesis, electric field probes and 3D thermometry are not available, leaving only temperature probes. Due to the longer scan

times in MRI, the heat diffusion must be considered when temperature probes are used to determine the local SAR [74]. To achieve this, a novel method for heat diffusion compensation is introduced in this section. This method compensates for the heat diffusion in the tip of a cone phantom during extended RF exposure through the application of Newton's law of cooling [81].

The results from Section 4.2 showed that a cone phantom can be used to replicate skin-bore contact cases. Thus, to determine the local SAR at the tip of a cone phantom from temperature measurements, several steps must be taken. For better understanding of the thermal dynamics during RF exposure, one can look at Figure 3.4. In this system, the tip of the cone phantom and the bulk (the larger bottom) are segregated. The assumption is made that the bulk temperature is unaffected by heat transfer with the tip and by RF exposure, since these factors are considered to have small effects on the temperature.

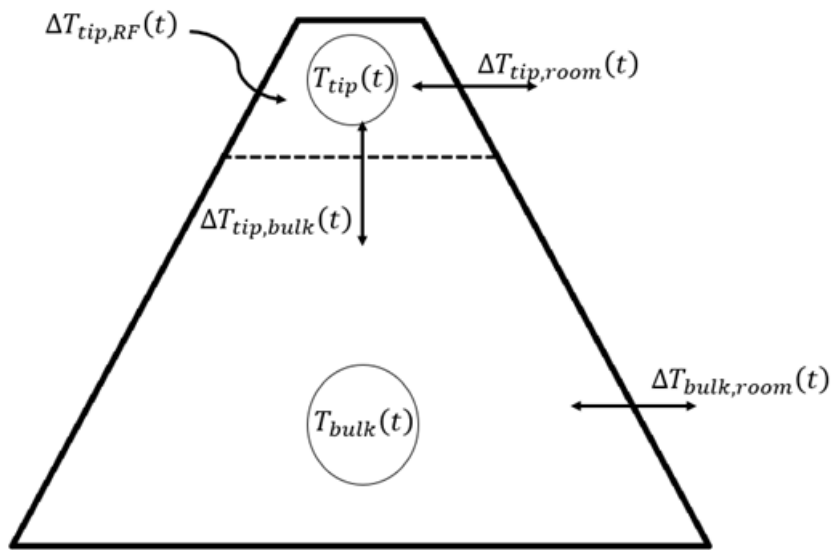


Figure 3.4: Schematic model of the thermal dynamics during RF exposure in the cone phantom. The circles represent the locations of the temperature probes in the tip and bulk.

The following variables and constants are used in the thermal model of the system:

$T_{tip}(t)$	Tip temperature over time
$T_{bulk}(t)$	Bulk temperature over time
$T_{0,tip}$	Tip temperature at the start of the measurement
$T_{0,bulk}$	Bulk temperature at the start of the measurement
T_{room}	Room temperature
$\Delta T_{tip,room}(t)$	Change in tip temperature due to heat transfer with the room over time
$\Delta T_{tip,bulk}(t)$	Change in tip temperature due to heat transfer with the bulk over time
$\Delta T_{tip,RF}(t)$	Change in tip temperature due to RF field absorption over time
$\Delta T_{bulk,room}(t)$	Change in bulk temperature due to heat transfer with the room over time
$T_{tip,room}(t)$	Tip temperature compensated for the room temperature over time
a	Constant of decay between room and tip temperature
b	Constant of decay between bulk and tip temperature

The schematic in Figure 3.4 shows that tip temperature is influenced by heat exchange from the room, bulk, and RF exposure, as outlined in Formula 3.1. The aim of the data analysis is

to isolate heat exchange due to the RF exposure ($\Delta T_{\text{tip,RF}}(t)$), from which the local SAR can be calculated.

$$T_{\text{tip}}(t) = T_{0,\text{tip}} + \Delta T_{\text{tip,room}}(t) + \Delta T_{\text{tip,bulk}}(t) + \Delta T_{\text{tip,RF}}(t) \quad (3.1)$$

To isolate the $\Delta T_{\text{tip,RF}}(t)$, predictions of the other heating factors must be made. Therefore, these other heating factors must be isolated. The first heating factor that can be isolated is the $\Delta T_{\text{tip,room}}(t)$. To achieve this, an additional assumption is made that the rate of change in temperature due to heat exchange with the room is uniform over the entire phantom, thus implying that $\Delta T_{\text{tip,room}}(t)$ is equal to $\Delta T_{\text{bulk,room}}(t)$ when $T_{\text{tip}}(t)$ and $T_{\text{bulk}}(t)$ are equal.

In a situation without RF exposure and with the previous made assumptions that the $T_{\text{bulk}}(t)$ does not change due to heat transfer with the tip, the $T_{\text{bulk}}(t)$ is only variable to $\Delta T_{\text{bulk,room}}(t)$ and can be described by Formula 3.2.

$$T_{\text{bulk}}(t) = T_{0,\text{bulk}} + \Delta T_{\text{bulk,room}}(t) \quad (3.2)$$

The cooling or warming of a body can be described by Newton's law of cooling, stating that the rate of temperature change of a body is proportional to the difference between its own and the ambient temperature. This difference decays exponentially as a function of time [81]. Using this law, Formula 3.3 can be formulated to describe the $T_{\text{bulk}}(t)$.

$$T_{\text{bulk}}(t) = T_{\text{room}} - (T_{\text{room}} - T_{0,\text{bulk}}) * e^{-a*t} \quad (3.3)$$

Where a is the exponential constant of decay due to the difference between the cone phantom and the room temperature.

As the assumption was made that the rate of change in temperature due to heat exchange with the room is uniform over the entire phantom, a can be applied as both the tip and bulk rate of temperature change. The change in tip temperature due to the difference with the room temperature can then be described by Formula 3.4.

$$\Delta T_{\text{tip,room}}(t) = - (T_{\text{room}} - T_{0,\text{tip}}) * e^{-a*t} + (T_{\text{room}} - T_{0,\text{tip}}) \quad (3.4)$$

Through Formula 3.4, the $T_{\text{tip}}(t)$ can be adjusted for $\Delta T_{\text{tip,room}}(t)$ in Formula 3.1, it is then only affected by heat exchange with the bulk and RF absorption.

$$T_{\text{tip}}(t) - \Delta T_{\text{tip,room}}(t) = T_{0,\text{tip}} + \Delta T_{\text{tip,bulk}}(t) + \Delta T_{\text{tip,RF}}(t) \quad (3.5)$$

The next step is to find a formula that describes $\Delta T_{\text{tip,bulk}}(t)$. This factor consists of the change in tip temperature due to heat transfer with the bulk over time, as the relatively large mass of the bulk compared to the tip will pull or add heat to the tip while a temperature difference between the two exists.

Again, applying Newton's law of cooling, $\Delta T_{\text{tip,bulk}}(t)$ can be formulated by an exponentially decaying function as previously used in Formula 3.3. Only now, instead of the constant T_{room} , the temperature of the body with which heat is exchanged is the variable $T_{\text{bulk}}(t)$.

$$\Delta T_{\text{tip,bulk}}(T_{\text{bulk}}, t) = -(T_{\text{bulk}}(t) - T_{0,\text{tip}}) * e^{-b*t} + (T_{\text{bulk}}(t) - T_{0,\text{tip}}) \quad (3.6)$$

Where b is the exponential constant of decay due to the difference between the tip and the bulk temperature.

Formula 3.6 is a function of both time and $T_{\text{bulk}}(t)$. To successfully implement Formula 3.6, it must only be a function of time. This can be solved by inserting Formula 3.3 into 3.6, which results into the following formula.

$$\Delta T_{\text{tip,bulk}}(t) = (T_{\text{room}} - T_{0,\text{bulk}}) * e^{-(a+b)*t} + (T_{0,\text{bulk}} - T_{\text{room}}) * e^{-a*t} + (T_{0,\text{tip}} - T_{\text{room}}) * \dots * e^{-b*t} + T_{\text{room}} - T_{0,\text{tip}} \quad (3.7)$$

With Formula 3.7, $T_{\text{tip}}(t)$ can be adjusted for both $\Delta T_{\text{tip,room}}(t)$ and $\Delta T_{\text{tip,bulk}}(t)$, now it is only dependent on heat generated by RF exposure.

$$T_{\text{tip}}(t) - \Delta T_{\text{tip,room}}(t) - \Delta T_{\text{tip,bulk}}(t) = T_{0,\text{tip}} + \Delta T_{\text{tip,RF}}(t) \quad (3.8)$$

Finally, it is possible to isolate the $\Delta T_{\text{tip,RF}}(t)$ factor.

$$\Delta T_{\text{tip,RF}}(t) = T_{\text{tip}}(t) - \Delta T_{\text{tip,room}}(t) - \Delta T_{\text{tip,bulk}}(t) - T_{0,\text{tip}} \quad (3.9)$$

In an MRI experiment the $\Delta T_{\text{tip,RF}}(t)$ should be calculated for each position separately. The SAR can be determined from $\Delta T_{\text{tip,RF}}(t)$ through the formula

$$SAR = \frac{\Delta T_{\text{tip,RF}} * C * 10^3}{\Delta t} \quad (3.10)$$

where C is the heat capacity, for an aqueous solution C is 4.178J/g °C [82]. Δt is the exposure time [83]. The last step in the data analysis is to normalise for the difference in RF averaged power transmitted between positions during an MRI experiment.

Values for a and b are determined through a measurement where the cone phantom is placed inside the MRI without RF exposure.

Constant a can be determined by fitting Formula 3.3 to $T_{\text{bulk}}(t)$ as measured inside an MRI without RF exposure. The fitting is performed by the 'fit' function in MATLAB 2021b [84]. The nonlinear least-squares method is applied to find a value for a that fits the $T_{\text{bulk}}(t)$ with the smallest error. $T_{0,\text{bulk}}$ is determined by averaging the first five values of $T_{\text{bulk}}(t)$ to filter white noise [85].

Constant b can be determined from a measurement inside an MRI bore without RF field exposure when a value for a is found. First, the $T_{\text{tip}}(t)$ must be compensated for $\Delta T_{\text{tip,room}}(t)$ through Formula 3.4, resulting in $T_{\text{tip,room}}(t)$. Then b is calculated by fitting Formula 3.11 to the compensated $T_{\text{tip,room}}(t)$, Formula 3.11 is derived by inserting Formula 3.7 into Formula 3.5, where $\Delta T_{\text{tip,RF}}(t)$ is equal to 0 due to the absence of RF exposure.

$$T_{\text{tip,room}}(t) = (T_{\text{room}} - T_{0,\text{bulk}}) * e^{-(a+b)*t} + (T_{0,\text{bulk}} - T_{\text{room}}) * e^{-a*t} + (T_{0,\text{tip}} - T_{\text{room}}) * \dots * e^{-b*t} + T_{\text{room}} \quad (3.11)$$

The results of this novel method for determining local SAR can be seen in Section 4.3.

3.4 MRI experiment

Research question 4 seeks to determine the location on the MRI bore where a patient would experience the highest contact heating. To answer this question, an in-vitro MRI experiment will be conducted. This experiment will utilize the cone phantom from research question 2, that was found to be able to mimic skin-bore contact cases in Section 4.2, and the method from Section 3.3 will be applied to determine local SAR at the contact point.

It is likely that the highest contact heating is measured near the capacitors of the birdcage transmission coil; however, their location is classified knowledge in modern MRI scanners. So, the highest heating locations must be found experimentally. To do this, the contact position on the bore wall is varied over the z-axis with the goal to identify the location of the end-rings. Additionally, the locations of the current feeding ports on the birdcage's end-rings are important, as these can increase the strength of the local electric field and subsequently induce higher local heating [35]. Varying the inclination at the end-rings on the bore wall might identify these port locations.

The MRI experiment is performed on a Siemens Magnetom Aera 1.5T MRI scanner at the MRI Labs of the University of Twente (Enschede, the Netherlands) at an RF frequency of 64MHz. The cone phantom from Section 3.2 is used in the MRI experiment and the geometric properties are identical to the simulated cone. A shell of the cone phantom is 3D printed with a thickness of 2mm. The shell is filled with an aqueous solution of 2g/L agar and 3.28g/L sodium chloride to mimic the properties of muscle tissue (ϵ : 72.2, σ : 0.688S/m) at the Larmor frequency of 64MHz [86, 87, 88].

During the experiment, the contact heating at a shift over the z-positions and angular inclination is investigated. To accomplish this, an MRI compatible arm is built that can be placed on the MRI table and can be adjusted to different inclination angles. The rotational axis of the arm is raised 13cm from the MRI table. The total length of the arm including the phantom is 34cm. A gear rack placed on the arm interacts with a gear rack at the base of the arm, the amount that the gear racks overlap influences the angle of the arm. The materials are multiplex wood plate (thickness: 10mm), round profile copper rods (diameter: 4mm), polyvinyl chloride tube (diameter: 60mm) and polyacetal racks. The arm construction with cone phantom can be seen in Figure 3.5a.

The cone phantom is exposed to an RF field emitted by the integrated RF birdcage body coil for 116 seconds at each position. The average RF power level varies between positions and is normalized in the data analysis. The z-positions are adjusted by shifting the MRI-table over distances of 20mm, from -500mm to 500mm, at a phantom arm inclination angle of 18°. The z-positions are in respect to the isocentre of the MRI scanner. The range of inclination angles will cover 216° and are evaluated at both of the suspected end-ring locations. Because the phantom arm construction has a range of 108°, the setup is rotated to acquire the additional 108° to 216° inclination range. The setup within the MRI scanner can be seen in Figure 3.5b and the inclination range of the arm can be seen in Figure 3.6. The phantom is placed on the table together with salt solution bottles to act both as weight to fixate the arm and to act as an RF field sink. During the measurements, the averaged RF power for each position was noted, the values of the centre B_1^+ field were not.

Two OpSense [89] fibre-optic temperature sensors are inserted into the phantom through two small holes drilled into the phantom shell, one in the tip and one in the lower bulk. The hole in the tip is approximately 1cm below the top of the cone. The temperature measurements are taken

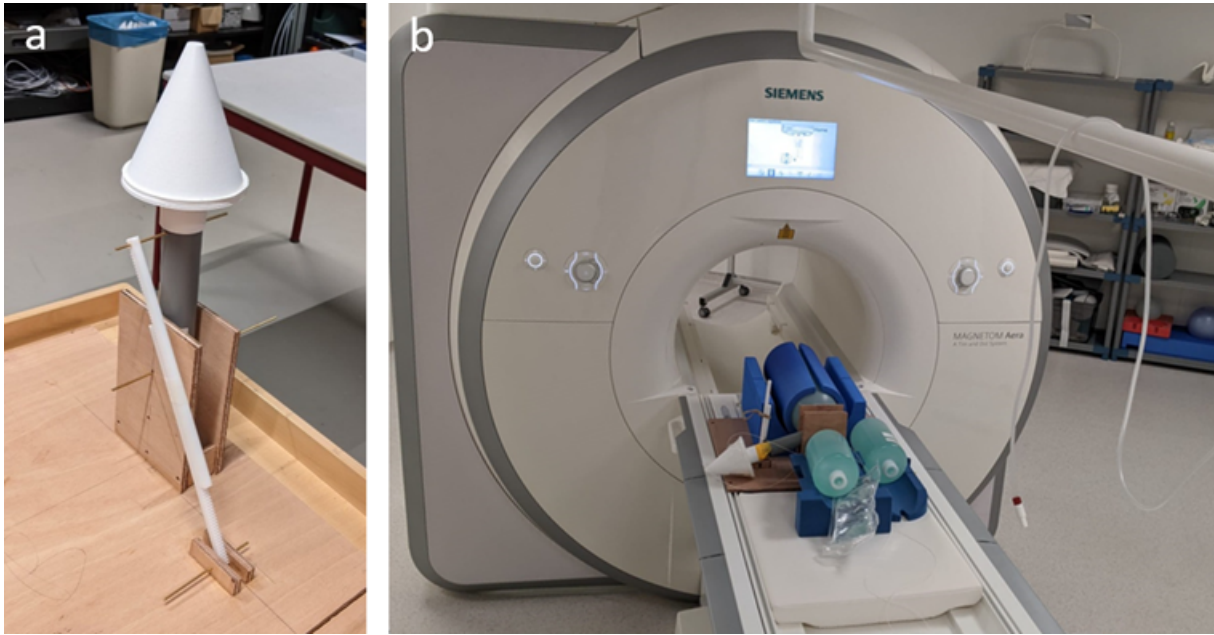


Figure 3.5: a) The angle adjustable MRI compatible arm with the cone phantom shell placed on top, at this instance the inclination angle is set to 108° . b) The phantom construction placed on the table of the MRI scanner.

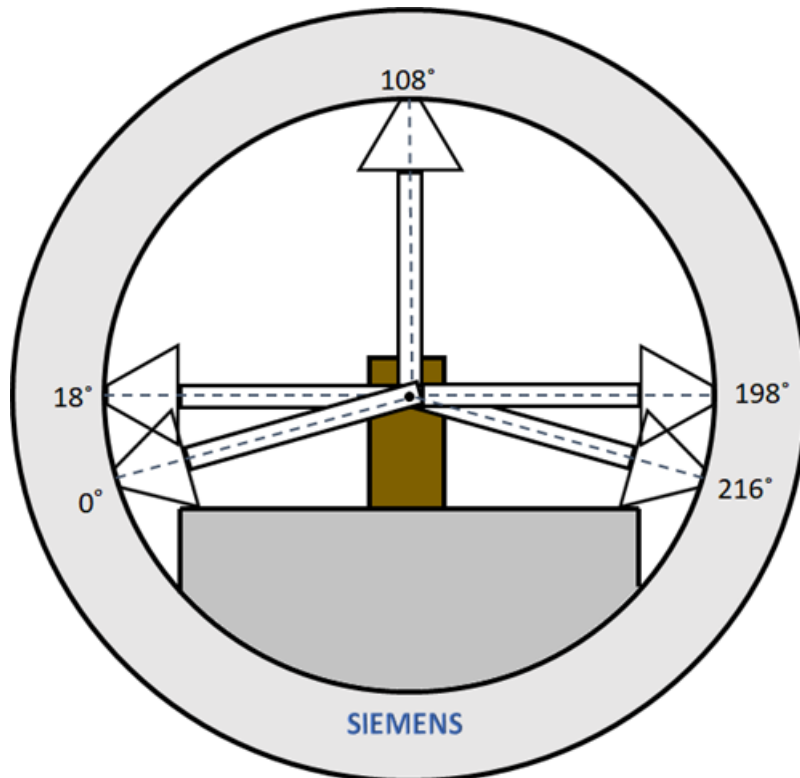


Figure 3.6: Schematic of the arm inclination angles within the MRI scanner.

at a frequency of 1 measurement per 1.4 seconds. The temperature sensors are connected to the OTG-MPK5 platform. The measurements for the local SAR determination constants a and b were taken on a different day than the MRI experiment itself. The MRI experiment results can be seen in Section 4.4.

4 RESULTS

The results are presented in four sections. The first section shows the skin-bore contact simulation results where the Gustav body model is shifted over the z- and x-positions. The second section shows the simulation results of the simplified phantoms. The third section shows the results of the novel method to measure SAR through heat diffusion compensation. The fourth section shows the results of the MRI experiment.

4.1 Simulation of skin-bore contact mechanism

In a birdcage, the strongest electric fields are near the end-rings of the transmission coil as shown in Figure 4.1c,d. Figure 4.1a illustrates how the bore wall shields the birdcage's electric field from travelling medially into the bore space, while the RF shield contains the electric field travelling laterally. The strongest electric fields are found near the capacitors of the birdcage as can be seen in Figure 4.1a,b. In Figure 4.1b,d the birdcage is loaded by the Gustav body model at a z-position of 250mm, where the peak SAR_{10g} is observed. When the body model is placed inside the birdcage, the electric field near the bore wall increases in strength by the presence of the electric conductor.

The influence of the skin-bore contact position on the intensity of SAR_{10g} is illustrated in Figure 4.2, which shows the Gustav body model at a z-position of 0mm, 205mm, 250mm and 345mm. In this figure a peak SAR_{10g} is observed at a shift of 250mm, the location closest to the birdcage's capacitor.

Figure 4.3 shows the peak SAR_{10g} values of the body model at the skin-bore contact point in relation to the z-position. It also contains the corresponding B_1^+ values at the birdcage centre versus the z-position. The SAR_{10g} peaks at 40.22W/kg at a z-position of 250mm, and centre B_1^+ field strength ranges from 2.484 μ T to 3.004 μ T.

Figure 4.4 shows the simulated peak SAR_{10g} values of the Gustav body model at the skin-bore contact point and corresponding B_1^+ centre value versus the x-position. The SAR_{10g} peaks at 40.22W/kg at a x-position of 0mm, the case of direct contact, and gradually decreases to 4.99W/kg at a x-position of 40mm. The centre B_1^+ values vary from 2.558 μ T to 2.884 μ T.

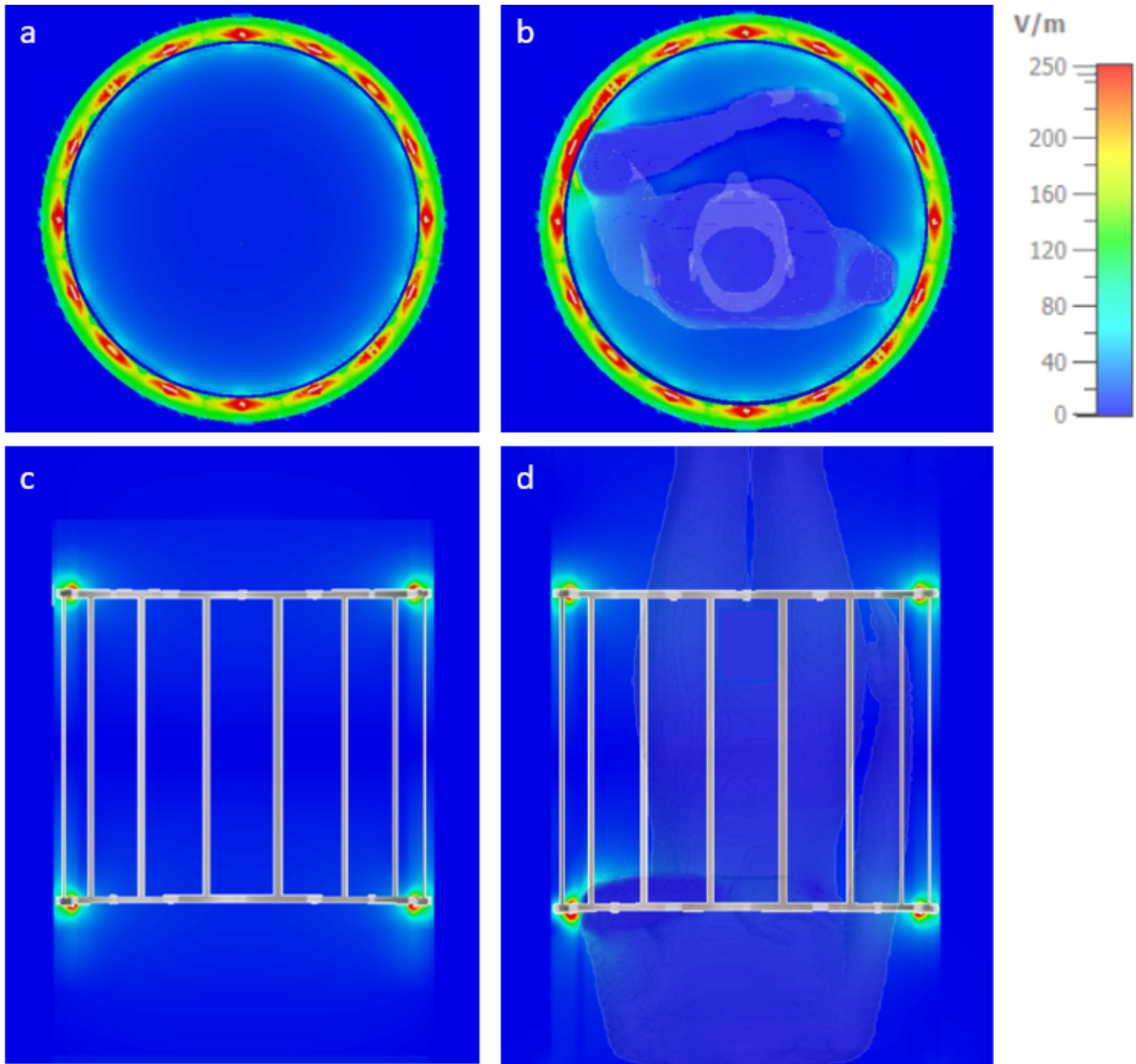


Figure 4.1: Electric strength field maps of an empty birdcage (a,c) and a birdcage loaded by the Gustav body model contacting the bore wall at a z-position of 250mm (b,d), where the peak SAR_{10g} is observed. The maps in the upper row (a,b) are a side view and the electric field is mapped on a xy-plane at z=250mm. The lower row (c,d) are a top view and the electric field is mapped on a xz-plane at y=118mm. Both these planes intersect the bore wall contact point.

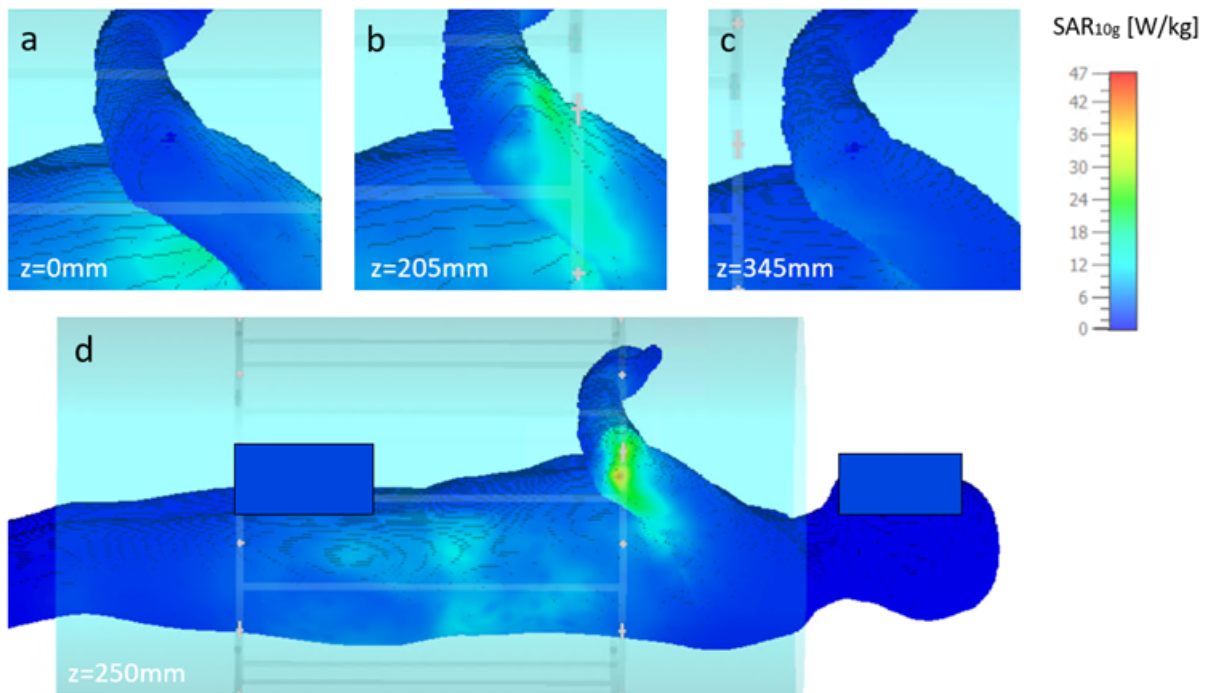


Figure 4.2: Simulated SAR_{10g} results for a range of z-positions. Shown are the SAR_{10g} of the Gustav's body model elbow contacting the bore wall at a z-position of a) 0mm, b) 205mm, c) 345mm and d) 250mm. A peak SAR_{10g} is observed at a shift of 250mm, the location closest to the birdcage's capacitor.

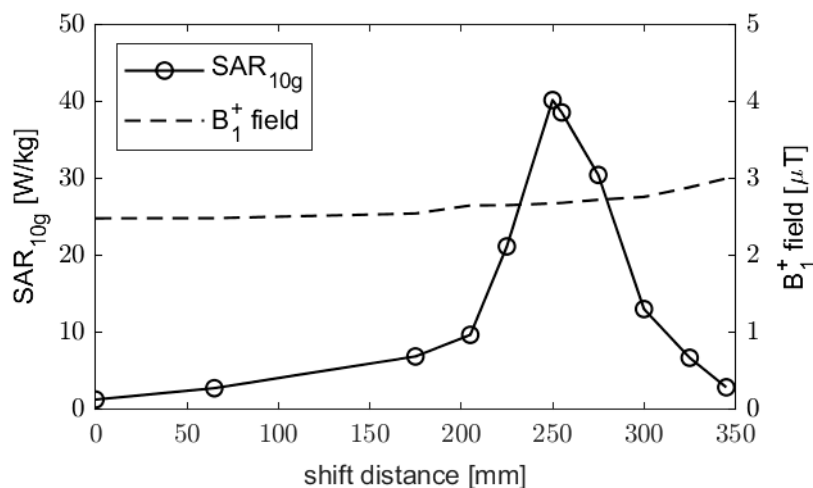


Figure 4.3: Simulated SAR_{10g} results for z-position shift of the Gustav body phantom. Shown are the simulated peak SAR_{10g} values at the skin-bore contact point and corresponding B_1^+ centre value versus the z-position. The results are obtained through normalization to 2W/kg whole-body SAR.

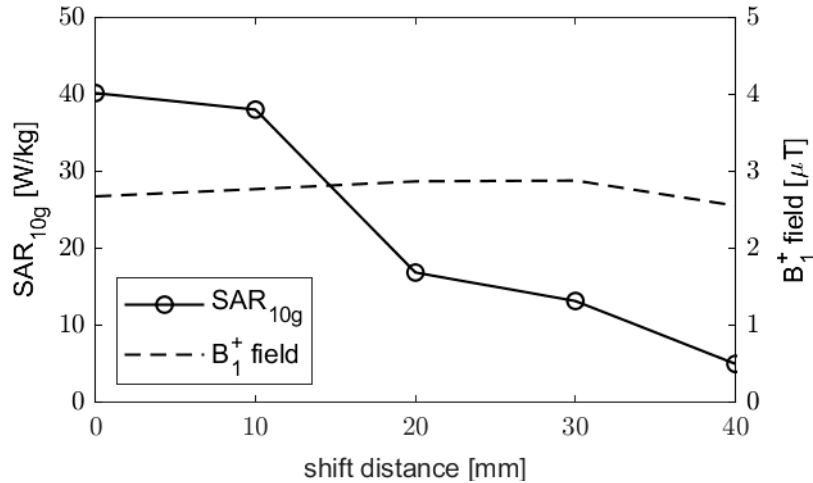


Figure 4.4: Simulated SAR_{10g} results for x-position shift of the Gustav body phantom. Shown are the simulated peak SAR_{10g} values at the skin-bore contact point and corresponding B₁⁺ centre value versus the z-position. The results are obtained through normalization to 2W/kg whole-body SAR.

4.2 Simplified phantom object

The influence that the phantom design has on the intensity of SAR_{10g} at the skin-bore contact point is illustrated in Figure 4.5, which compares the SAR_{10g} of the Gustav body phantom, the simplified arm and elbow phantoms and the cone phantom at a z-position shift of 250mm. In this figure a peak SAR_{10g} is visible for all phantoms at the skin-bore contact point, the overall highest SAR_{10g} is observed on the Gustav body phantom.

Table 4.1 shows the SAR_{10g} at the bore wall contact point and B₁⁺ field centre strength of the phantoms at a z-position of 250mm. The data is normalised to 2W/kg whole-body SAR. The data shows that the SAR_{10g} and B₁⁺ field centre strength reduce by 51.5% and 21.9%, respectively, when the Gustav body phantom is compared to the cone phantom. The SAR_{10g} decreases between the Gustav body model and simplified arm phantom, but stays approximately equal between the simplified arm and elbow phantoms. SAR_{10g} decreases further between the simplified elbow and cone phantom.

Table 4.1: Simulated SAR_{10g} and B₁⁺ field centre strength results for the different phantom types. The SAR_{10g} and B₁⁺ field centre strength values are normalized to 2W/kg whole-body SAR.

Phantom Type	SAR _{10g} [W/kg]	B ₁ ⁺ [μT]
Gustav Body 2.0mm	40.223	2.679
Arm Phantom	25.624	2.079
Elbow Phantom	26.053	2.391
Cone Phantom	19.490	2.110

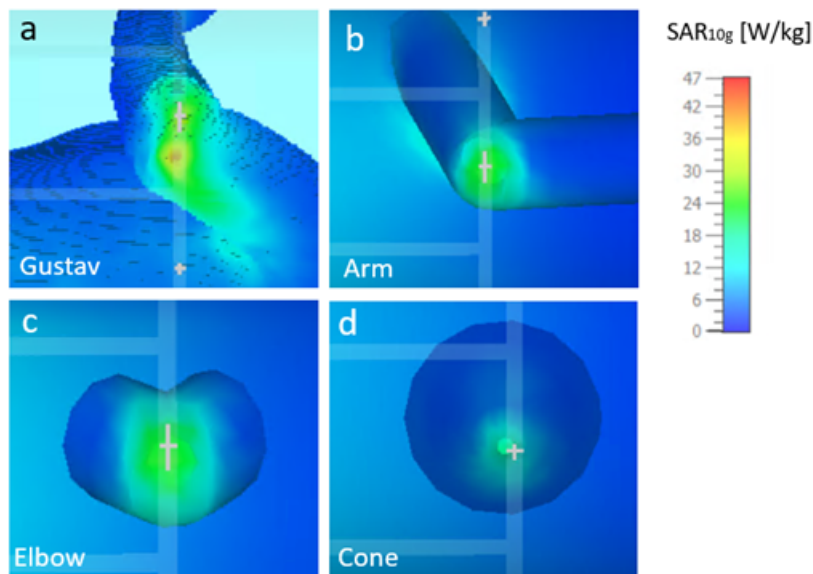


Figure 4.5: Simulated SAR_{10g} results for different phantoms. Shown are the SAR_{10g} of the a) Gustav's body model, b) simplified arm phantom, c) simplified elbow phantom and d) cone phantom at a z-position of 250mm. The highest observed SAR_{10g} is visible on the Gustav body model.

4.3 Local SAR measurement

The temperature of the MRI room is 18°C. Figure 4.6a shows the temperature measurement of the cone phantom inside the MRI scanner without RF exposure. Constant a is determined by fitting Formula 3.3 to the $T_{\text{bulk}}(t)$, visible in Figure 4.6b. The best fitting value for a is $1.124 \cdot 10^{-4}$, with an R^2 of 0.9999.

The tip temperature is adjusted for heat exchange with the room to determine the constant b . This value is found by fitting Formula 3.11 to the revised tip temperature, resulting in a best fit for constant b of $4.961 \cdot 10^{-5}$ with an R^2 value of 0.8849.

The room and bulk temperature of a cone phantom, with no RF exposure, was measured a second time. Figure 4.7 shows the compensation of heat diffusion, obtained by applying the method from Section 3.3 and the found values for a and b .

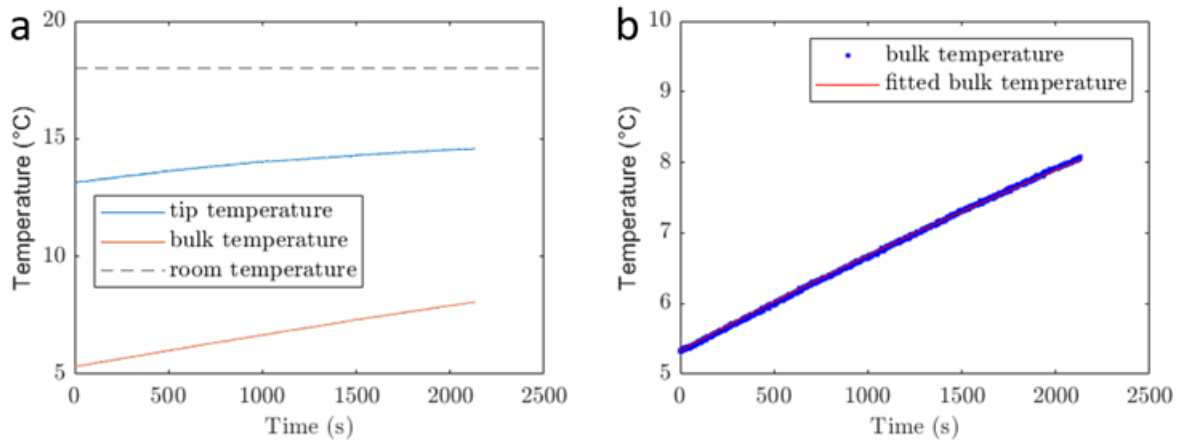


Figure 4.6: a) Temperature measurements of the cone phantom without RF exposure; b) result of the fitting method on the bulk temperature.

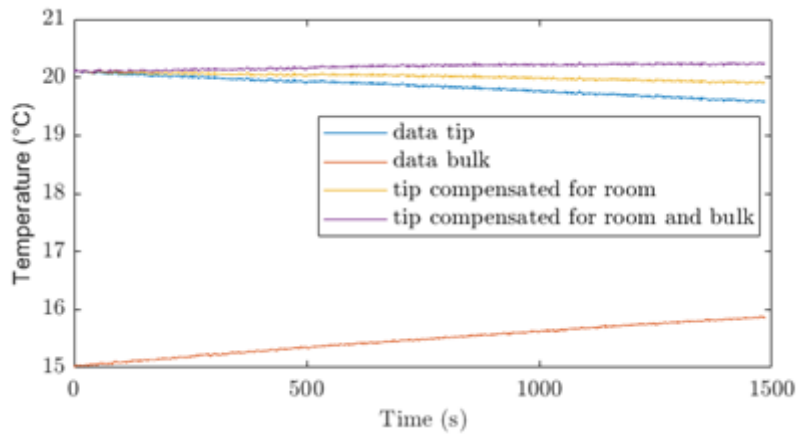


Figure 4.7: Temperature measurement of the cone phantom without RF exposure. The 'data tip' is the measured temperature in the tip of the cone and 'data bulk' the temperature in the bulk. The 'tip compensated for room' and 'tip compensated for room and bulk' lines are the tip temperatures compensated for heat exchanges with only the room and both the room and bulk, respectively. As both the room and bulk temperature are lower than the tip temperature, they both have a cooling effect. The compensated lines will be higher than the measured tip temperature for in these lines the cooling effect has been removed. The combined compensation for room and bulk results in an approximately constant temperature value as all thermodynamic factors in the tip of the cone have been compensated for.

4.4 MRI experiment

Figure 4.8 shows two temperature measurements taken during the MRI experiment. In Figure 4.8a the cone phantom was shifted over the z-positions and in Figure 4.8b inclined from 0° to 108° while at a z-position of 220mm. Three peaks can be observed in the tip temperature measurement for the z-position shift. While changing the inclination, the tip temperature presents a stair-like pattern. Due to reaching the maximum whole-body SAR, the MRI scanner prohibited scanning further than a z-position of 380mm.

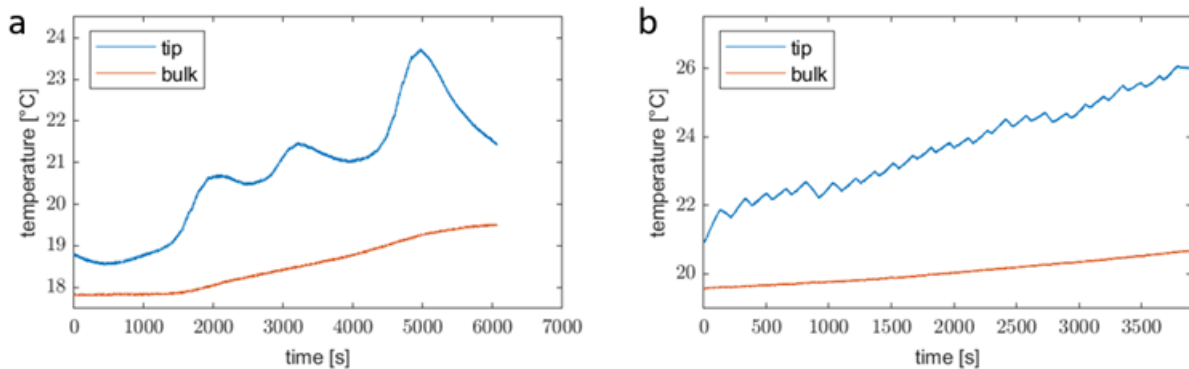


Figure 4.8: MRI experiment temperature measurements. Shown are the temperature measurements of the cone phantom a) shifted over the z-positions and b) over the inclination angle from 0° to 108° at a z-position of 220mm.

Figure 4.9a shows the temperature change in the cone tip between the start and end of RF exposure at each z-position. Three peaks are visible, while some z-positions display a decrease in temperature during active RF exposure. The average RF power sent by the MRI scanner is also plotted against the temperature change. Figure 4.9b shows the tip temperature change adjusted to account for heat diffusion following the methods from Section 3.3 and normalised to an average RF transmit power of 193.2W. The 'factor=1' line is the adjusted data with values of a and b found in Section 4.3. Nonetheless, the temperature change at a number of z-positions is still below 0°C , which contradicts the fact that RF exposure can only add heat energy. Therefore, a and b were multiplied by a factor of 5.5 to acquire adjusted temperature change data that is positive for each z-position.

Figures 4.10 and 4.11 demonstrate the results of the MRI experiment. Section 3.3's method was used to adjust the data for heat diffusion, but with the in Section 4.3 found constants a and b multiplied by 5.5. The highest temperature change of 1.46°C is observed at -240mm z-position and 128° inclination angle, corresponding to a SAR value of 52.66W/kg .

Figure 4.10 shows the temperature change and the corresponding SAR over the range of z-positions. Three peaks are present in the data. The first peak is located at -240mm and has a SAR value of 26.38W/kg . The second peak is situated at -40mm and has a SAR value of 21.29W/kg . The third peak lies at 220mm , with a SAR value of 41.13W/kg .

Figure 4.11 shows the temperature change and corresponding SAR over the range of inclination angles. The two z-positions over which the inclination angles were changed, correspond to the outer two heating peaks in Figure 4.10, suspected to be the end-ring locations. SAR values ranged from 23.62W/kg to 52.66W/kg at z-position of -240mm and from 22.54W/kg to 42.60W/kg at a z-position of 220mm .

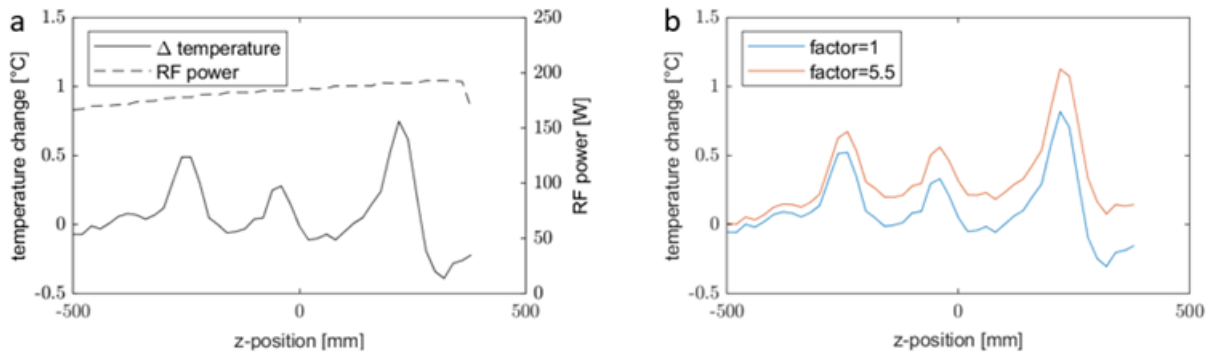


Figure 4.9: MRI experiment data: a) Shown is the tip temperature change between the start and end of RF exposure at each z-position. Additionally, the average RF power transmitted by the MRI scanner is plotted along the tip temperature change. b) Shown is the tip temperature change adjusted for heat diffusion and average transmitted RF power.

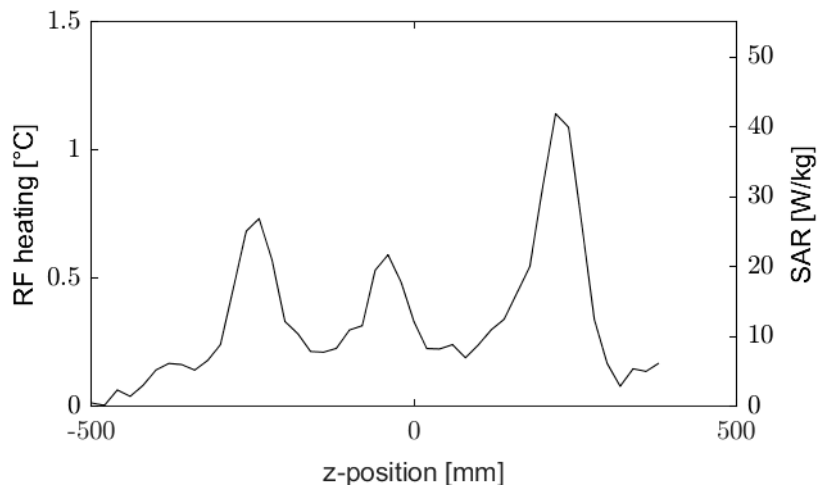


Figure 4.10: MRI experiment: temperature change due to the RF exposure and the corresponding SAR over the range of z-positions at an inclination of 18°.

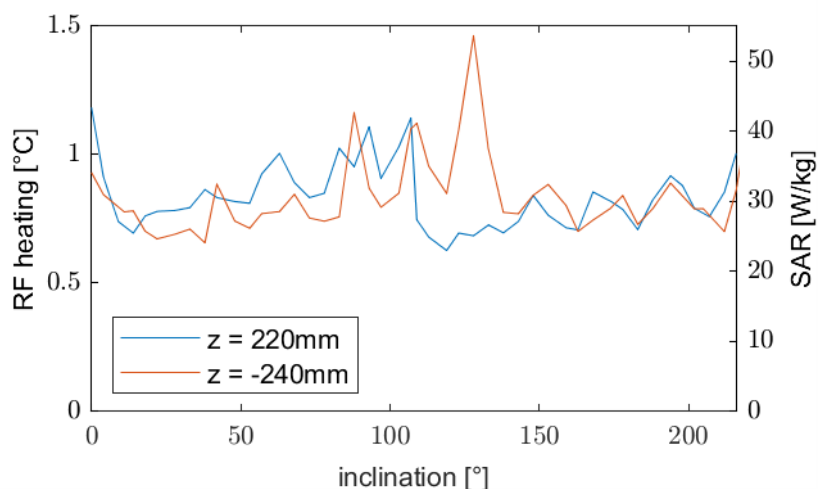


Figure 4.11: MRI experiment: temperature change due to the RF exposure and the corresponding SAR over the range of inclination angles at the suspected end-ring locations.

5 DISCUSSION

This chapter will discuss the results of Chapter 4.

5.1 Simulation of skin-bore contact mechanism

Research question 1 investigates the mechanism of skin-bore contact injuries and in Section 2.4 it was found that stray electric fields might be the cause. These fields arise from the stray capacitance between the birdcage's coil capacitors and nearby electric conductors. Therefore, it is likely that highest local SAR can be found near the capacitors on the bore wall, independent from skin-bore contact since the stray fields can move inward towards nearby conductors.

Figure 4.1 shows the simulation results of an empty birdcage and one loaded by the Gustav body phantom. Figure 4.1a shows that the bore wall shields the electric field of an empty birdcage from travelling medially into the bore space, while the RF shield prevents it from travelling laterally. In Figure 4.1b, the electric field travelling inward is substantially stronger than in Figure 4.1a, particularly at the contact point. This is in line with the hypothesis that stray electric fields are generated between capacitors and nearby electric conductors like human bodies during MRI scanning.

Simulations of the Gustav body phantom with z-position and x-position shifts are in accordance with the hypothesis of stray electric fields. Figure 4.3 shows a peak SAR_{10g} of 40.22W/kg at a z-position of 250mm at the location in front of a capacitor. Figure 4.4 reveals that the peak SAR_{10g} is found during contact with the bore wall, but is also high 10mm from the bore wall, with approximately half of the SAR_{10g} left at 20mm and a quarter at 30mm. The data confirms that contact with the bore wall is not necessary for higher SAR_{10g} values on the elbow, although SAR_{10g} does decrease with an increasing gap from the bore wall.

The results of these simulations are in line with the only simulation-based study that focused on skin-skin and skin-bore contact. Tang et al. [6] found a peak SAR_{10g} of 48W/kg near the capacitor of an 8-rung resonant HP birdcage during skin-bore contact. This is close to the SAR_{10g} of 40.22W/kg found in this thesis. They found a SAR_{10g} of 10W/kg at a z-position of 0mm, while this thesis found a value of 1.26W/kg. This discrepancy can be explained by the expected error in the middle region of the 16-rung non-resonant HP birdcage utilized in this thesis [35].

Additionally, Tang et al. [6] claimed their simulated SAR_{10g} exceeded the highest safety limit of partial-body SAR, which is 10W/kg in the normal mode (Table 2.1). Yet, SAR_{10g} and partial-body SAR are two distinct parameters; SAR_{10g} is a local one, with no safety limits in body coils, and partial-body SAR is global. Thus, their claim that the simulated SAR_{10g} surpasses partial-body SAR limits, although true, holds little value.

Simulations in Section 4.1 demonstrate that stray electric fields generated between the capacitors of the birdcage and nearby electric conductors can be the mechanism responsible for skin-

bore contact injuries. The SAR_{10g} level needed to induce burn injuries and other influencing factors were not investigated in this thesis. Even so, for the creation of a phantom to measure local SAR at a skin-bore contact point inside an MRI scanner, these stray electric fields must be taken into account as the mechanism behind skin-bore contact injuries.

5.2 Simplified phantom object

Research question 2 seeks to find a simplified phantom, which can accurately replicate the RF absorption characteristics of the human elbow in a skin-bore contact case. Because the mechanism of stray electric fields was uncovered in Research question 1, it is hypothesized that adjustments from a body phantom to a simplified phantom are primarily affected by adjustments in close proximity to the capacitors of a birdcage, as it is here that stray electric fields interact with the tissue. Simulation data from Table 4.1 shows that SAR_{10g} at the contact point decreases between the Gustav body model and the simplified arm phantom, but remains approximately equal between the simplified arm and elbow phantoms, and decreases again from the simplified elbow to the cone phantom.

The first simplification step from the Gustav body model to the simplified arm phantom is made to reduce the complexity of the phantom. The simulated SAR_{10g} at the skin-bore contact point is reduced by 36.5% (Table 4.1). The centre B_1^+ field value is also reduced by 22.4%. The decrease in SAR_{10g} could be due to a weaker B_1^+ field or a simpler elbow geometry, but it is unclear which of the two factors has a larger impact.

The second simplification step from the simplified arm phantom to the elbow phantom is made to investigate whether the heating at the skin-bore contact point is influenced by a connection with the body cylinder. Simulations indicated a 1.7% increase in SAR_{10g} at the skin-bore contact point, suggesting negligible influence from a connection with the body cylinder (Table 4.1). This is expected as the phantom characteristics and geometry near the contact point were consistent between the two simulations.

The last simplification step is made from the simplified elbow phantom to the cone phantom to obtain a geometric cone object as a phantom. The simulated SAR_{10g} at the skin-bore contact point was reduced by 25.2% (Table 4.1). This is a substantial reduction as the material properties and degree of complexity are similar for both phantoms. However, the difference could be explained in part by the reduction in surface area contacting the bore wall as seen in Figure 4.5. As SAR_{10g} is averaged over 10 grams of tissue, the centre mass of the nearest 10 grams of tissue would be further from the bore wall in a phantom with a subsequently reduced contact area. The stray electric field strength decreases with distance from the capacitor, thus inducing less SAR_{10g} in the cone phantom.

Simulation results indicate that a cone phantom can feasibly model the physical characteristics of a skin-bore contact case. However, the simulated SAR_{10g} at the bore wall contact point decreases by 51.5% compared to the Gustav body model. To increase the SAR_{10g} at the contact point, it could be considered to increase the contact area or to increase the permittivity material properties. For now it is assumed that the cone phantom can imitate a human elbow, but the local SAR values should not be expected to be accurate.

5.3 Local SAR measurement

Research question 3 is about finding a method to measure local SAR. In Section 3.3 a novel approach for assessing local SAR in a cone phantom is presented. Figure 4.7 demonstrates

that the presented method can account for heat diffusion in the tip with the room and bulk of the cone phantom. Without RF exposure and after application of the heat diffusion model, the temperature in the cone tip remains constant, validating the accuracy of this approach.

However, the application to the MRI experiment data in Section 4.4 revealed problems in the method. Primarily, temperature change values remained negative at some z-positions after heat diffusion compensation, as seen in Figure 4.9b. This would imply that RF exposure is cooling the tip, because the minimal temperature change would be 0°C in the case of no RF exposure. To rectify this, the a and b constants were multiplied by a factor of 5.5.

The reason why the constants had to be corrected is uncertain, yet it is plausible that the data being measured over two days is a contributing factor. On the first day, the data was measured from which the a and b constants were calculated; on the second day, the MRI experiment data for Section 4.4 was collected. On this second day, the temperature probes had to be re-inserted into the cone phantom, which could introduce a variation in probe depth between the two days. A temperature probe with a shallower depth would measure a higher diffusion rate by the room, rendering the constants inaccurate for the second day's measurements.

Calculating values for parameters a and b with Formulas 3.3 and 3.11 requires knowledge of the application of mathematical models. This model compensates for both the heat diffusion with the room and the cone's bulk using two constants. To make the method more accessible, it might be possible to reduce the number of constants to one. Creating a constant and subsequent model that can directly approximate the combined heat diffusion with the room and bulk. This would likely lower the model's precision, but the payoff may be worth obtaining a simpler application of the model.

It should be noted that this model is not limited to skin-bore contact cases, but could also be used in other phantom cases to calculate local SAR or validate simulations. However, to validate simulations, a normalization method is still needed between the accepted RF power in the simulation and the transmitted power in the MRI scanner. This model is potentially advantageous to research groups with limited technical capabilities, as only two temperature probes are required.

5.4 MRI experiment

Research question 4 seeks out to find the location of maximal local SAR on the MRI bore wall. Results in Figures 4.10 and 4.11 show that the local SAR on the bore wall is more dependent on z-position than inclination, with the highest SAR of 52.66W/kg at a -240mm z-position and 128° inclination.

Figure 4.10 indicates that there are three local SAR peaks along the z-positions: two end-ring peaks and one unexpected peak in the middle. This differed from the simulated results in Figure 11, which showed only a peak at the end-ring. Although the computational birdcage model is known to be inaccurate in the middle [35], the simulation result is corroborated by the study by Tang et al. [6], who also simulated skin-bore contact cases and likewise only found a local SAR peak at the end-ring. This implies that the Siemens Magnetom Area 1.5T scanner has potentially a third stray electric field source between the two end-rings, likely applying a hybrid BP birdcage coil as the RF transmission coil. However, due to the classified nature of the hardware in the Siemens MRI scanners, it is not possible to confirm this assumption.

Figure 4.11 indicates that the local SAR near the end-rings of the birdcage does not strongly

vary with inclination. While the local SAR fluctuates, no successive values of high local SAR can be identified that would indicate a peak over the inclination. Because now a single local SAR peak could be attributed to a potential error in the measurements. This implies that single capacitors or current feeding port locations cannot be defined on the end-rings with these inclination step sizes. Additionally, by analysing only an inclination range of 216° , a 144° 'blind spot' exists that allows the feeding ports to remain hidden, as these would only be parted by a gap of 90° .

The only other study that simulated skin-bore contact cases by Tang et al. [6] also conducted thermal simulations of the tissue heating. They found that 15 minutes of RF exposure could raise tissue temperature to 76°C , and only 1 minute of RF exposure could lead to a 51°C temperature, an increase of 14°C from the body temperature of 37°C . The authors said that these temperature increases 'clearly proved skin-bore contact burn injuries in silica'. However, their simulations were not validated by an MRI experiment. The results in Section 4.4 found a maximal tissue temperature increase of only 1.46°C , over a 116-second RF exposure period. This observation is substantially lower than the simulation by Tang et al. predicts, even considering that the cone phantom underestimates the local SAR by 51.5% (Table 4.1). Therefore, the potential hazard of skin-bore contact injuries might be lower than the study by Tang et al. would like to believe, also confirming the importance of validating electromagnetic simulations.

The results in Section 4.4 show that the in this thesis developed method to measure RF induced heating and local SAR at skin-bore contact points works. The method requires only basic materials and can produce the location of the highest RF induced heating with only two temperature probes, basic materials and a 3D printed phantom shell.

6 FUTURE WORK AND RECOMMENDATIONS

When writing this thesis, a special emphasis was put into detailing the proposed method for measuring local SAR at skin-bore contact points, so that other researchers can learn and use this information for their own purposes. This chapter outlines ways to improve the method further and provides the author's outlook for future research in this subject.

To enhance the proposed method, I recommended to reduce the inclination step size if the goal is to search for locations of high RF heating on the bore wall. Additionally, I recommended to conduct an experiment comparing RF heating in the tip of the cone phantom to that of a biological sample that would better replicate human tissue. This experiment would aim to validate whether the cone phantom's properties can accurately replicate those of a human elbow in a skin-bore contact case.

The developed method for measuring local SAR and compensating for heat diffusion can be a complex process to implement, but it could be applied to a greater range of MRI cases. To make it more attainable, it may be possible to reduce the constants to one and create a model that combines the heat diffusion with the room and phantom bulk. This would likely reduce the precision of the model, but the payoff may be worth obtaining a simpler application of the model.

A natural progression of this work is to analyse whether the local SAR values on the bore wall pose an actual risk for the patient. Therefore, also MRI scanners with stronger magnetic fields need to be considered, as these potentially induce stronger stray electric fields. This with the goal to identify whether the current safety procedures of non-conducting pads are sufficient when the number and static magnetic fields strength of MRI scanners will increase in the coming years.

This research also showed that it is important that simulation-based studies always reflect on the validity of their results. Simulation-based studies are important as a fast and cost-effective method of local heating determination. But simulation methods should be validated before the results can be assumed predictive for heating experienced by patients in MRI scanners.

7 CONCLUSION

The main goal of this thesis is to develop a method to measure the local SAR at skin-bore contact points. With skin-bore injury cases expected to rise in the future, it seeks to advance the research on skin-bore contact injuries as yet little is known about the causal mechanism and patient risk.

The results have shown that stray electric fields generated between the capacitors of the bird-cage and a nearby electric conductor can be the causal mechanism responsible for skin-bore contact injuries. This implies that also close proximity to the bore wall near the capacitor can cause excessive local heating. It has also shown that a cone phantom can replace a human elbow in skin-bore contact cases, although there is a potential decrease of 51.5% in measured SAR_{10g}. A novel method has been developed that uses two temperature probes to measure local SAR and compensate for the heat diffusion. Combining these results a phantom-based method has been developed that can measure RF induced heating and local SAR at skin-bore contact points in an MRI scanner.

The thesis contributes to the understanding of skin-bore contact injuries through identifying the causal mechanism and providing an accessible method for researchers and MRI technicians to measure local SAR on the bore wall. Also the developed method for measuring local SAR through two temperature probes might be applicable to experiments outside the context of skin-bore contact cases.

To conclude, the goal set out for thesis is achieved and the developed method to measure RF induced heating and local SAR at skin-bore contact points can be assumed to work. The challenge now will be to identify the patient risk of skin-bore contact injuries and to assess whether the current safety procedures of non-conducting pads are sufficient when the number and static magnetic fields strength of MRI scanners will increase in the coming years.

REFERENCES

- [1] Wilfried Andrä and Hannes Nowak. *Magnetism in Medicine: A Handbook*. 2007.
- [2] Food and Drug Administration (FDA). Mri: Benefits and risks. <https://www.fda.gov/radiation-emitting-products/mri-magnetic-resonance-imaging/benefits-and-risks>, 9 2017. Accessed: 2022-10-16.
- [3] G. Chaljub, L. A. Kramer, R. F. Johnson, Jr Johnson, H. Singh, and W. N. Crow. Projectile cylinder accidents resulting from the presence of ferromagnetic nitrous oxide or oxygen tanks in the mr suite. *American Journal of Roentgenology*, 177, 2001.
- [4] Medicines and Healthcare Products Regulatory Agency. Safety guidelines for magnetic resonance imaging equipment in clinical use, 2021.
- [5] Adriaan Moelker, Piotr A. Wielopolski, and Peter M. T. Pattynama. Acoustic noise and related safety considerations in mr imaging environments. *Practical MR Safety Considerations for Physicians, Physicists, and Technologists*, pages 123–137, 2001.
- [6] Electromagnetic simulation of rf burn injuries occurring at skin-skin and skin-bore wall contact points in an mri scanner with a birdcage coil. *Physica Medica*, 82, 2021.
- [7] Paul T. Hardy and Kathleen M. Weil. A review of thermal mr injuries. *Radiologic technology*, 81, 2010.
- [8] Tsukasa Doi, Yuya Yamatani, Tsuyoshi Ueyama, Shigeo Nishiki, Akio Ogura, Hideaki Kawamitsu, Toshio Tsuchihashi, Tomoyuki Okuaki, Tsuyoshi Matsuda, and Masayuki Kumashiro. [an investigative report concerning safety and management in the magnetic resonance environment: there are more accidents than expected]. *Nihon Hoshasen Gijutsu Gakkai zasshi*, 67, 2011.
- [9] Mary F. Dempsey, Barrie Condon, and Donald M. Hadley. Investigation of the factors responsible for burns during mri. *Journal of Magnetic Resonance Imaging*, 13, 2001.
- [10] Lisa Mittendorff, Adrienne Young, and Jenny Sim. A narrative review of current and emerging mri safety issues: What every mri technologist (radiographer) needs to know. *Journal of Medical Radiation Sciences*, 69, 2022.
- [11] Mri-related fda adverse event reports: A 10-yr review. *Medical Physics*, 46, 2019.
- [12] Mordor Intelligence. Magnetic resonance imaging (mri) market - growth, trends, covid-19 impact, and forecasts (2022-2027), 2021.
- [13] Grand View Research. Magnetic resonance imaging market size, share trends analysis report by architecture, by field strength, by application (brain neurological, spine musculoskeletal), by end-use, by region, and segment forecasts, 2021 - 2028, 12 2020.

- [14] NOS Binnenland Redactie. Nederland krijgt scherpste mri-scanner ter wereld. <https://nos.nl/artikel/2464575-nederland-krijgt-scherpste-mri-scanner-ter-wereld>. Accessed: 2023-02-21.
- [15] Mirco Cosottini and Luca Roccatagliata. Neuroimaging at 7 t: are we ready for clinical transition? *European Radiology Experimental*, 5, 2021.
- [16] Giuseppe Barisano, Farshid Sepeshband, Samantha Ma, Kay Jann, Ryan Cabeen, Danny J. Wang, Arthur W. Toga, and Meng Law. Clinical 7 t mri: Are we there yet? a review about magnetic resonance imaging at ultra-high field. *British Journal of Radiology*, 92, 2019.
- [17] Rijksinstituut voor Volksgezondheid en Milieu (RIVM). Echografie en mri. <https://www.rivm.nl/medische-stralingstoepassingen/trends-en-stand-van-zaken/diagnostiek/echografie-en-mri>. Accessed: 2022-03-19.
- [18] Paul A. Bottomley. Turning up the heat on mri. *Journal of the American College of Radiology*, 5, 2008.
- [19] Taiki Yamaguchi, Yuichiro Abe, Yoshio Ichino, Shigenobu Satoh, Takeshi Masuda, Shoichi Kimura, Manabu Ito, and Toru Yamamoto. Heating sensation in patients with and without spinal fixation devices during mri examination at different magnetic field strengths. *Journal of Magnetic Resonance Imaging*, 49, 2019.
- [20] Valentina Hartwig, Giulio Giovannetti, Nicola Vanello, Massimo Lombardi, Luigi Landini, and Silvana Simi. Biological effects and safety in magnetic resonance imaging: A review. *International Journal of Environmental Research and Public Health*, 6, 2009.
- [21] Frank C. Shellock and John V. Crues. Mr procedures: Biologic effects, safety, and patient care. *Radiology*, 232, 2004.
- [22] Peter Nordbeck, Florian Fidler, Ingo Weiss, Marcus Warmuth, Michael T. Friedrich, Philipp Ehse, Wolfgang Geistert, Oliver Ritter, Peter M. Jakob, Mark E. Ladd, Harald H. Quick, and Wolfgang R. Bauer. Spatial distribution of rf-induced e-fields and implant heating in mri. *Magnetic Resonance in Medicine*, 60, 2008.
- [23] Christopher J. Yeung, Robert C. Susil, and Ergin Atalar. Rf heating due to conductive wires during mri depends on the phase distribution of the transmit field. *Magnetic Resonance in Medicine*, 48, 2002.
- [24] Peter L. Davis, Charles Shang, Lalith Talagala, and A. William Pasculle. Magnetic resonance imaging can cause focal heating in a nonuniform phantom. *IEEE Transactions on Biomedical Engineering*, 40, 1993.
- [25] Cristina Armenean, Emmanuel Perrin, Mircea Armenean, Olivier Beuf, Frank Pilleul, and Hervé Saint-Jalmes. Rf-induced temperature elevation along metallic wires in clinical magnetic resonance imaging: Influence of diameter and length. *Magnetic Resonance in Medicine*, 52, 2004.
- [26] Sukhoon Oh, Yeun Chul Ryu, Giuseppe Carluccio, Christopher T. Sica, and Christopher M. Collins. Measurement of sar-induced temperature increase in a phantom and in vivo with comparison to numerical simulation. *Magnetic Resonance in Medicine*, 71, 2014.
- [27] International Electrochemical Commission. Medical electrical equipment: part 2-33. particular requirements for the safety of magnetic resonance equipment for medical diagnosis. *IEC 60601-2-33*, 2010.

- [28] Wyger M. Brink, Sahar Yousefi, Prernna Bhatnagar, Rob F. Remis, Marius Staring, and Andrew G. Webb. Personalized local sar prediction for parallel transmit neuroimaging at 7t from a single t1-weighted dataset. *Magnetic Resonance in Medicine*, 88, 2022.
- [29] Sheikh Faisal Ahmad, Young Cheol Kim, Ick Chang Choi, and Hyun Deok Kim. Recent progress in birdcage rf coil technology for mri system. *Diagnostics*, 10, 2020.
- [30] J. W. Hand, Y. Li, E. L. Thomas, M. A. Rutherford, and J. V. Hajnal. Prediction of specific absorption rate in mother and fetus associated with mri examinations during pregnancy. *Magnetic Resonance in Medicine*, 55, 2006.
- [31] Hiroyuki Muranaka, Takayoshi Horiguchi, Yoshitake Ueda, and Nobuyoshi Tanki. Evaluation of rf heating due to various implants during mr procedures. *Magnetic Resonance in Medical Sciences*, 10, 2011.
- [32] Henry S. Ho. Safety of metallic implants in magnetic resonance imaging. *Journal of Magnetic Resonance Imaging*, 14, 2001.
- [33] Nicole Hadert, Qi Liu, and Waldemar Zylka. Numerical examinations of simplified spondylosis models concerning energy absorption in magnetic resonance imaging. *Current Directions in Biomedical Engineering*, 2, 2016.
- [34] Cecil Guclu, George Kashmar, Avadis Hacinliyan, and Orhan Nalcioglu. An fem approach for the characterization of the rf field homogeneity at high field. *Magnetic Resonance in Medicine*, 37, 1997.
- [35] Elena Lucano, Micaela Liberti, Gonzalo G. Mendoza, Tom Lloyd, Maria Ida Iacono, Francesca Apollonio, Steve Wedan, Wolfgang Kainz, and Leonardo M. Angelone. Assessing the electromagnetic fields generated by a radiofrequency mri body coil at 64 mhz: Defeating versus accuracy. *IEEE Transactions on Biomedical Engineering*, 63, 2016.
- [36] Gašper Podobnik. Two cases of mri-induced skin burns. *Medical Imaging and Radiotherapy Journal*, 37, 10 2020.
- [37] Laura Tagell, Ahmad Alcheikh, Richard Jurevics, and Anish Puliyayil Nair. Thigh burn – a magnetic resonance imaging (mri) related adverse event. *Radiology Case Reports*, 15, 2020.
- [38] Nicole S. Mandel, Jeremy L. Ramdial, and Erin N. Marcus. A second-degree burn after mri. *Cleveland Clinic Journal of Medicine*, 84, 2017.
- [39] Jerry L. Prince and Jonathan Links. Medical imaging signals and systems. *Isbn 0-13-065353-5*, 2014.
- [40] Lars G. Hanson. Is quantum mechanics necessary for understanding magnetic resonance? *Concepts in Magnetic Resonance Part A: Bridging Education and Research*, 32, 2008.
- [41] Christopher M. Collins and Zhangwei Wang. Calculation of radiofrequency electromagnetic fields and their effects in mri of human subjects. *Magnetic Resonance in Medicine*, 65, 2011.
- [42] Manushka V. Vaidya, Christopher M. Collins, Daniel K. Sodickson, Ryan Brown, Graham C. Wiggins, and Riccardo Lattanzi. Dependence of b1- and b1+ field patterns of surface coils on the electrical properties of the sample and the mr operating frequency. *Concepts in Magnetic Resonance Part B: Magnetic Resonance Engineering*, 46, 2016.

- [43] Manual J. Murbach. Emf risk assessment: Exposure assessment and safety considerations in mri and other environments, 2013.
- [44] Bernhard Gruber, Martijn Froeling, Tim Leiner, and Dennis W.J. Klomp. Rf coils: A practical guide for nonphysicists. *Journal of Magnetic Resonance Imaging*, 48, 2018.
- [45] Cecil E. Hayes, William A. Edelstein, John F. Schenck, Otward M. Mueller, and Matthew Eash. An efficient, highly homogeneous radiofrequency coil for whole-body nmr imaging at 1.5 t. *Journal of Magnetic Resonance (1969)*, 63, 1985.
- [46] Cecil E. Hayes. The development of the birdcage resonator: A historical perspective. *NMR in Biomedicine*, 22, 2009.
- [47] Cecil E Hayes. 4694255 radio frequency field coil for nmr. *Magnetic Resonance Imaging*, 6, 1988.
- [48] C. N. Chen, D. I. Hoult, and V. J. Sank. Quadrature detection coils—a further $\sqrt{2}$ improvement in sensitivity. *Journal of Magnetic Resonance (1969)*, 54, 1983.
- [49] Nicola De Zanche and Klaas P. Pruessmann. Algebraic method to synthesize specified modal currents in ladder resonators: Application to noncircular birdcage coils. *Magnetic Resonance in Medicine*, 74:1470–1481, 11 2015.
- [50] IEC. International electrotechnical commission. <http://www.iec.ch/>. Accessed: 2022-10-11.
- [51] A. Ahlbom, U. Bergqvist, J. H. Bernhardt, J. P. Cesarini, L. A. Court, M. Grandolfo, M. Hietanen, A. F. McKinlay, M. H. Repacholi, D. H. Sliney, J. A.J. Stolwijk, M. L. Swicord, L. D. Szabo, M. Taki, T. S. Tenforde, H. P. Jammet, and R. Matthes. Guidelines for limiting exposure to time-varying electric, magnetic, and electromagnetic fields (up to 300 ghz). *Health Physics*, 74:494–521, 1998.
- [52] Domenico Formica and Sergio Silvestri. Biological effects of exposure to magnetic resonance imaging: An overview. *BioMedical Engineering Online*, 3, 2004.
- [53] C. K. Chou, H. Bassen, J. Osepchuk, Q. Balzano, R. Petersen, M. Meltz, R. Cleveland, J. C. Lin, and L. Heynick. Radio frequency electromagnetic exposure: Tutorial review on experimental dosimetry. *Bioelectromagnetics*, 17, 1996.
- [54] ACR Committee on MR Safety. Manual on mr safety, 2020.
- [55] Faculty of Clinical Radiology. Mri safety guidelines, 2021.
- [56] the Society and College of Radiographs. Safety in magnetic resonance imaging, 2021.
- [57] COMSOL Inc. Comsol multiphysics. <http://www.comsol.com/>. Accessed: 2022-10-13.
- [58] Zurich Med Tech. Sim4life. <http://www.zmt.swiss/sim4life/>. Accessed: 2022-10-13.
- [59] Dassault Systems. Cst studio suite. <https://www.3ds.com/products-services/simulia/products/cst-studio-suite/>. Accessed: 2022-10-13.
- [60] Craig Warren, Silvestar Sesnic, Alessio Ventura, Lara Pajewski, Dragan Poljak, and Antonios Giannopoulos. Comparison of time-domain finite-difference, finite-integration, and integral-equation methods for dipole radiation in half-space environments. *Progress In Electromagnetics Research M*, 57, 2017.
- [61] Zhabiz Rahimi. The finite integration technique (fit) and the application in lithography simulations, 2011.

- [62] René Marklein. The finite integration technique as a general tool to compute acoustic , electromagnetic , elastodynamic , and coupled wave fields. *Review of Radio Science: 1999-2002 URSI*, 2002.
- [63] T Weiland. A discretization model for the solution of maxwell's equations for six-component fields. *Archiv Elektronik und Uebertragungstechnik*, 31, 1977.
- [64] Abdel Monem M. El-Sharkawy, Di Qian, Paul A. Bottomley, and William A. Edelstein. A multichannel, real-time mri rf power monitor for independent sar determination. *Medical Physics*, 39, 2012.
- [65] John P. Stralka and Paul A. Bottomley. A prototype rf dosimeter for independent measurement of the average specific absorption rate (sar) during mri. *Journal of Magnetic Resonance Imaging*, 26, 2007.
- [66] Jihong Wang. Issues with radiofrequency heating in mri. *Journal of Applied Clinical Medical Physics*, 15, 2014.
- [67] Youngseob Seo and Zhiyue J. Wang. Measurement and evaluation of specific absorption rate and temperature elevation caused by an artificial hip joint during mri scanning. *Scientific Reports*, 11, 2021.
- [68] Youngseob Seo. An mri scanner-independent radiofrequency dosimeter for the estimation of rf power deposition with a human torso phantom. *Concepts in Magnetic Resonance Part B: Magnetic Resonance Engineering*, 47B, 2017.
- [69] Di Qian, Abdel Monem M. El-Sharkawy, Paul A. Bottomley, and William A. Edelstein. An rf dosimeter for independent sar measurement in mri scanners. *Medical Physics*, 40, 2013.
- [70] Thomas Schmid, Oliver Egger, and Niels Küster. Automated e-field scanning system for dosimetric assessments. *IEEE Transactions on Microwave Theory and Techniques*, 44, 1996.
- [71] Desmond T.B. Yeo, Zhangwei Wang, Wolfgang Loew, Mika W. Vogel, and Ileana Hancu. Local specific absorption rate in high-pass birdcage and transverse electromagnetic body coils for multiple human body models in clinical landmark positions at 3t. *Journal of Magnetic Resonance Imaging*, 33, 2011.
- [72] R. B. Roemer, A. M. Fletcher, and T. C. Cetas. Obtaining local sar and blood perfusion data from temperature measurements: steady state and transient techniques compared. *International Journal of Radiation Oncology, Biology, Physics*, 11, 1985.
- [73] Yoshinobu Okano and Hironobu Shimoji. Comparison measurement for specific absorption rate with physically different procedure. *IEEE Transactions on Instrumentation and Measurement*, 61, 2012.
- [74] Leeor Alon, Daniel K. Sodickson, and Cem M. Deniz. Heat equation inversion framework for average sar calculation from magnetic resonance thermal imaging. *Bioelectromagnetics*, 37, 2016.
- [75] Leeor Alon, Gene Cho, Leslie F. Greengard, Ricardo Otazo, Daniel K. Sodickson, and Cem D. Deniz. Calculation of 10g average sar via inversion of the heat equation using mri thermometry and thermal property measurements. *Int Soc Magn Reson Med*, 2014.
- [76] John De Poorter, Carlos De Wagter, Yves De Deene, Carsten Thomsen, Freddy Ståhlberg, and Eric Achten. Noninvasive mri thermometry with the proton resonance frequency (prf) method: In vivo results in human muscle. *Magnetic Resonance in Medicine*, 33, 1995.

- [77] Wyger M. Brink, Zhiyi Wu, and Andrew G. Webb. A simple head-sized phantom for realistic static and radiofrequency characterization at high fields. *Magnetic Resonance in Medicine*, 80, 2018.
- [78] W. Liu, C. M. Collins, and M. B. Smith. Calculations of b1 distribution, specific energy absorption rate, and intrinsic signal-to-noise ratio for a body-size birdcage coil loaded with different human subjects at 64 and 128 mhz. *Applied Magnetic Resonance*, 29, 2005.
- [79] Dassault Systems. Cst voxel family. https://space.mit.edu/RADIO/CST_online/merged-Projects/3D/common_tools/common_tools_biomodels.htmVoxel_Family. Accessed: 2022-10-24.
- [80] Marija Nikolovski. Detailed modeling of the human body in motion to investigate the electromagnetic influence of fields in a realistic environment, 2017.
- [81] Colm T. O’Sullivan. Newton’s law of cooling—a critical assessment. *American Journal of Physics*, 58, 1990.
- [82] ITIS Foundation. Itis heat capacity. <https://itis.swiss/virtual-population/tissue-properties/database/heat-capacity/>. Accessed: 2022-11-10.
- [83] Leeor Alon, Gene Y. Cho, Xing Yang, Daniel K. Sodickson, and Cem M. Deniz. A method for safety testing of radiofrequency/microwave-emitting devices using mri. *Magnetic Resonance in Medicine*, 74, 2015.
- [84] The Mathworks. Matlab 2021b. <https://nl.mathworks.com/products/matlab.html>. Accessed: 2022-10-09.
- [85] Gjerrit Meinsma, Ciska Heida, and Michel van Putten. Advanced techniques for signal analysis reader, 5 2021.
- [86] ITIS Foundation. Itis dielectric properties. <https://itis.swiss/virtual-population/tissue-properties/database/dielectric-properties/>. Accessed: 2022-11-07.
- [87] Qi Duan, Jeff H. Duyn, Natalia Gudino, Jacco A. De Zwart, Peter Van Gelderen, Daniel K. Sodickson, and Ryan Brown. Characterization of a dielectric phantom for high-field magnetic resonance imaging applications. *Medical Physics*, 41, 2014.
- [88] National Institutes of Health. Dielectric phantom recipe generator. <https://amri.ninds.nih.gov/cgi-bin/phantomrecipe>. Accessed: 2022-11-07.
- [89] OpSens Medical. Opsense. <https://opsensmedical.com/oem-solutions/products/fiber-optic-temperature-sensors/otg-mpk5/>. Accessed: 2022-11-07.